

***In vivo* 3D ultrasound computed tomography of musculoskeletal tissues with generative neural physics**

Zhijun Zeng^{1,2,3†}, Youjia Zheng^{1,2†}, Chang Su^{4,5†}, Qianhang Wu^{1,2}, Hao Hu^{1,2},
Zeyuan Dong^{4,6}, Shan Gao⁷, Yang Lv⁷, Rui Tang⁸, Ligang Cui⁸,
Zhiyong Hou⁹, Weijun Lin^{4,5}, Zuoqiang Shi^{10,11*}, Yubing Li^{4,6*}, He Sun^{1,2*}

¹College of Future Technology, Peking University, Beijing& 100871, China.

²National Biomedical Imaging Center, Peking University, Beijing& 100871, China.

³Department of Mathematical Sciences, Tsinghua University, Beijing& 100084, China.

⁴Institute of Acoustics, Chinese Academy of Sciences, Beijing& 100190, China.

⁵School of Physical Sciences, University of Chinese Academy of Sciences, Beijing& 100040, China.

⁶School of EECE, University of Chinese Academy of Sciences, Beijing& 100040, China.

⁷Department of Orthopedics, Peking University Third Hospital, Beijing& 100191, China.

⁸Department of Ultrasound, Peking University Third Hospital, Beijing& 100191, China.

⁹Department of Orthopaedic Surgery, The Third Hospital of Hebei Medical University,
Shijiazhuang& 050051, China.

¹⁰Yau Mathematical Sciences Center, Tsinghua University, Beijing& 100084, China.

¹¹Yanqi Lake Beijing Institute of Mathematical Sciences and Applications, Beijing& 101408, China.

*Corresponding author. Z. Shi: zqshi@tsinghua.edu.cn, Y. Li: liyubing@mail.ioa.ac.cn, H. Sun: hesun@pku.edu.cn

[†]These authors contributed equally to this work.

Abstract: Ultrasound computed tomography (USCT) is a radiation-free, high-resolution modality but remains limited for musculoskeletal imaging due to conventional ray-based reconstructions that neglect strong scattering. We propose a generative neural physics framework that couples generative networks with physics-informed neural simulation for fast, high-fidelity 3D USCT. By learning a compact surrogate of ultrasonic wave propagation from only dozens of cross-modality images, our method merges the accuracy of wave modeling with the efficiency and stability of deep learning. This enables accurate quantitative imaging of *in vivo* musculoskeletal tissues, producing spatial maps of acoustic properties beyond reflection-mode images. On synthetic and *in vivo* data (breast, arm, leg), we reconstruct 3D maps of tissue parameters in under ten minutes, with sensitivity to biomechanical properties in muscle and bone and resolution comparable to MRI. By overcoming computational bottlenecks in strongly scattering regimes, this approach advances USCT toward routine clinical assessment of musculoskeletal disease.

Introduction

Ultrasound Computed Tomography (USCT) is a promising medical imaging technology that combines the safety, portability, and affordability of traditional ultrasound with high-resolution 3D imaging capabilities. Unlike conventional B-mode ultrasound (1), which forms images solely based on echoes from tissue interfaces, USCT utilizes specialized transducer arrays—often annular, cylindrical, or hemispherical—to collect both transmitted and reflected waves from the scattering media (Fig. 1). USCT array emits waves sequentially from each transducer and records the corresponding signals from all transducers, enabling it to reconstruct the internal structure of biological tissues in a tomographic fashion (2). This technique is particularly advantageous for imaging tissues in high contrast and high resolution and for detecting abnormalities such as tumors (3–5). Additionally, USCT avoids the risks associated with ionizing radiation (used in X-ray CT) or magnetic fields (used in MRI), making it a safer alternative for patients like pregnant women, children, or individuals with magnetic foreign bodies (6).

Despite these advantages, the clinical adoption of USCT has been limited by the immense computational demands associated with its image reconstruction process. At the core of USCT reconstruction lies a complex inverse problem known as Full Waveform Inversion (FWI) (7), whose goal is to recover the acoustic properties of the tissue (e.g., sound speed, density and attenuation) with high resolution, potentially at sub-wavelength scales, from the recorded wavefields. Mathematically, the FWI problem can be formulated as a nonlinear Partial Differential Equation (PDE)-constrained optimization problem:

$$\min_{c, u_k} \sum_{k=1}^K \|y_k - u_k(x_f)\|_2^2, \quad \text{s.t.} \quad \left[\nabla^2 + \left(\frac{\omega}{c(x)} \right)^2 \right] u_k(x) = -\rho_k(x), \quad (1)$$

where c is the sound speed distribution in biological tissue, u_k is the full acoustic wavefield, $y_k \in \mathbb{C}^K$ is the recorded wavefield data of total K transducers, x defines the spatial coordinates within the computational domain, x_f defines the transducer locations, ω is the angular frequency of acoustic wavefield, ρ_k are the source terms, and k indexes the different transducers. FWI relies on solving a large number of wave equations in its forward and inverse process, simulating how waves propagate through a medium and iteratively refining the medium's parametric model until the simulated data aligns with the recorded data (Fig. 1c). Solving this problem is particularly computationally demanding in complex, large-scale, strongly scattering media, since any numerical method requires a significant number of elements or grid points per wavelength to capture high-frequency wave characteristics and achieve the desired level of accuracy (8). This high computational complexity has emerged as a substantial obstacle in clinical USCT, particularly in 3D imaging scenarios, such as full-leg scans to monitor bone and muscle diseases or whole-brain imaging for stroke diagnosis (6).

Recent research has explored deep learning models to mitigate these challenges in USCT. Existing deep learning solutions can be broadly categorized into two classes. The first approach endeavors to learn an end-to-end network that directly models the mapping from wavefield measurements to tissue's material properties. Existing work has designed various network architectures—including convolutional neural networks (CNNs), unrolled networks, and physics-inspired neural operators (9–12)—to infer tissue properties from wave signals without resorting to PDE solvers. However, these methods often overfit to the patterns inherent in synthetic training images rather than capturing the fundamental wave physics, leading to reconstruction artifacts that compromise their clinical reliability (13, 14). The second method involves physics-informed neural

networks (PINNs) (15, 16), which directly incorporate PDE constraints (such as governing equations, boundary conditions, and conservation relations) as training losses to simultaneously fit both the solutions and the unknown coefficients in PDE inverse problems. This approach explicitly regularizes the deep learning solutions to match the underlying physics. However, due to their inherent bias toward learning low-frequency features, PINNs struggle to capture highly oscillatory wave phenomena, limiting their ability to achieve high-resolution imaging over large fields of view in clinical USCT (17).

Here we propose a generative neural physics framework that integrates generative AI with neural PDE solvers to enable rapid, high-fidelity 3D USCT imaging (Fig. 1). The framework addresses two longstanding challenges in deploying deep learning for medical ultrasound: the simulation-to-reality gap between training datasets and real-world applications, and the difficulty of accurately and efficiently solving high-frequency, oscillatory wave PDEs under experimental conditions. Our approach begins by generating anatomically realistic, large-scale human organ phantoms (e.g., breasts, arms, legs) with accurate acoustic properties using physics-based style transfer of X-ray CT images and generative AI-driven data augmentation. These phantoms are used in a high-fidelity USCT simulator to produce multi-frequency wavefields. We then develop the Strong Scattering Neural Operator (S^2NO), a neural operator specifically designed for highly oscillatory PDEs on large computational domains. By embedding the governing physics of wave propagation into its architecture, S^2NO enables accurate and efficient modelling of multiple scattering events in clinical settings, establishing it as a versatile wave foundation model. Finally, we integrate S^2NO into a neural FWI framework, achieving MRI-comparable 3D reconstructions within minutes. This constitutes a Reality-to-Simulation-to-Reality (Real2Sim2Real) pipeline: (1) creating a realistic USCT simulation database from patient CT images (Reality-to-Simulation), and (2) enabling *in vivo*, high-resolution USCT imaging via a physics-informed neural PDE solver trained solely on synthetic data (Simulation-to-Reality).

Using this approach, we have successfully demonstrated *in vivo*, high-resolution, 3D USCT imaging of bone-containing human organs—a challenge long considered beyond ultrasound’s capabilities—with MRI comparable image quality. Moreover, we have reduced the computational time from several hours to under 10 minutes without sacrificing resolution. This breakthrough paves the way for the widespread clinical adoption of USCT.

Result

We apply our generative neural physics framework to USCT imaging across multiple human organs, evaluating its performance in both simulated and real-world scenarios. In this section, we first outline the Reality-to-Simulation stage, which generates a comprehensive USCT dataset of human organ phantoms and their corresponding wavefields under experimental settings. Following this, we introduce the S^2NO and validate its application in neural FWI using synthetic data. Finally, we demonstrate the Simulation-to-Reality stage, showing the high-fidelity rapid imaging of multiple human organs, especially the first MRI-standard *in vivo* 3D USCT imaging of musculoskeletal tissues (arms and legs).

USCT Dataset with Realistic Anatomy and Experimental Scenario

The success of deep learning models for medical imaging hinges on access to large amounts of realistic training data. Unlike CT or MRI, conventional ultrasound lacks standardized tomographic anatomy image databases, and although USCT offers a promising solution, limited system deployment and inefficient solvers make large-scale human organ dataset acquisition impractical. It is therefore essential to develop strategies that augment the limited existing datasets to a scale sufficient for effectively training deep learning models.

To address this challenge, we developed an innovative Real2Sim strategy that combines cross-modality clinical images with a foundation generative model to produce anatomically and physically realistic USCT phantoms (Fig.2). In this pipeline, clinical images (e.g., X-ray CT) or digital organ models were first segmented into tissue types—skin, fat, muscle, bone, and others—using the Segment Anything Model (SAM) (18), and each segment was assigned a sound speed based on tissue-specific acoustic properties (see Methods). This process yielded a small but anatomically and physically realistic dataset of USCT phantoms. Although too limited to train a generative model from scratch, these datasets enabled fine-tuning of the foundation generative model, Stable Diffusion (19), transferring anatomical knowledge into the model to generate diverse and realistic digital organ phantoms (Supplementary Note 5). As shown in Fig. 2, the original pre-trained model only produced semantically meaningful but anatomically incorrect structures (Fig. 2a), whereas the fine-tuned model accurately captured anatomical features while introducing medically plausible

variations to enhance data diversity (Fig. 2b).

We further simulated wavefields corresponding to the generated phantoms using a realistic USCT instrument simulator powered by an accurate numerical solver (CBS (20)) (Fig. 1b). Together, the synthetic phantoms and simulated measurements provide a critical foundation for training and evaluating next-generation USCT imaging algorithms.

S^2NO for Wave Simulation and USCT Reconstruction

Using the comprehensive AI-generated USCT, we then designed a novel neural PDE solver based on physical principles to achieve accurate wave propagation simulations and perform FWI in clinical trials. As shown in Fig. 3a and outlined in the Methods section, S^2NO implicitly incorporates an iterative variant of the wave equation to capture the complex multiple scattering effects in human tissue, which is particularly challenging in the presence of bone and dense soft tissue structures. To ensure that our models accurately capture fundamental wave propagation physics and generalize effectively to unseen real-world data, they were trained jointly on the entire multi-organ datasets. Details of the training methodology and implementation are provided in Methods and Supplementary Note 3.

Forward Simulation. We first evaluated the accuracy of S^2NO in simulating acoustic wavefields for synthetic breast, arm, and leg phantoms, using solutions from numerical solvers (CBS) as ground truth. Fig. 3b compares wavefield predictions at 0.6 MHz for representative phantoms using various neural operators. S^2NO outperformed the Fourier Neural Operator (FNO) (21), DeepONet (22) and U-Net (23), accurately capturing complex scattering patterns, such as those at bone-muscle interface and within marrow cavity of the femur. Supplementary Table S6-S8 summarize the quantitative performance of S^2NO and baseline methods across multiple organ types. While competing neural network methods struggled with tackling highly oscillatory scenarios in PDE solutions, S^2NO consistently achieved simulation accuracy comparable to traditional solvers. In addition to delivering superior accuracy, S^2NO also exhibited significant computational speedups and stability. As shown in Supplementary Table S10, S^2NO achieved 25~34 times faster simulation speed than the numerical solver for musculoskeletal tissues on an NVIDIA A800-80GB GPU, making it suitable for clinical USCT trials.

FWI Reconstruction. We then evaluated neural operator surrogates for reconstructing images from simulated observations of synthetic phantoms. A gradient-based FWI approach derived from the adjoint method, detailed in Supplementary Note 2, was employed. Ultrasonic signals at multiple frequencies (0.3MHz to 0.6MHz for breasts and 0.25MHz to 0.6MHz for arms and legs) were leveraged, progressively moving from low to high frequencies to enhance reconstruction accuracy (24).

Figure 4 compares FWI results for breast, arm, and leg phantoms obtained using conventional numerical solver (CBS), S^2NO , and other neural operators. Quantitative evaluation metric (SSIM) demonstrates that S^2NO -based FWI achieved reconstruction quality comparable to that of CBS and outperformed other neural operators across all phantom types (Fig. 4b,c and Supplementary Table S9). Specifically, S^2NO effectively recovered anatomical features—including skin, muscle, fat, and bone—with enhanced clarity. For breast phantoms exhibiting weaker scattering, S^2NO predicted more accurate high-frequency information compared to other baseline methods, resulting in sharper resolution at interfaces. For arm and leg phantoms that exhibit stronger scattering, S^2NO more accurately modelled multiple scattering phenomena, thus capturing bone morphology with improved fidelity and effectively suppressing scattering-induced imaging artifacts observed in other baselines’ reconstructions. Notably, during reconstruction, S^2NO tended to underestimate bone thickness, whereas the numerical solver typically overestimated it. Given its faster forward simulation, S^2NO -based FWI reduced the reconstruction time by up to fourteen-fold compared to traditional FWI methods (Supplementary Table S11).

***In Vivo* Human Breasts**

We first applied S^2NO -based FWI to two open-source *in vivo* breast USCT datasets from the Karmanos Cancer Institute (IRB Approval No. 040912M1) (3) to validate the model trained in Real2Sim stage. The datasets correspond to breasts with benign and malignant lesions. Acoustic signals across 7 frequencies (0.3 MHz to 0.6 MHz) were used to reconstruct sound speed distributions.

As shown in Fig. 5, S^2NO -based reconstructions captured detailed breast structures, including skin, glandular tissue, tumors, ductal networks, and fatty regions. Compared to conventional

delay-and-sum (DAS) (25, 26) and time-of-flight tomography (ToFT) (27) algorithms, S^2NO -based FWI produced higher-resolution images of interior structures with a parameter-free resolution (28) of approximately 1.36 mm, approaching the theoretical FWI limit (half the highest-frequency ultrasound wavelength) but cutting computation time 6-fold versus conventional numerical solvers. Importantly, Fig. 5e,f show that S^2NO -based FWI concretely distinguished malignant masses—characterized by irregular boundary morphology and a higher sound speed (~ 1590 m/s)—from benign lesions, which display regular boundaries and a lower sound speed (~ 1560 m/s), thereby underscoring the potential of our approach for efficient and accurate breast disease detection. Notably, the experimental apparatus used for imaging the breast was not identical to the settings employed in the simulation data (e.g., transducer locations), revealing the exceptional generalization capability of S^2NO to different hardware settings.

***In Vivo* 3D Human Arms**

We further applied our method to *in vivo* USCT arm data (0.25 MHz to 0.6 MHz), collected from two adult volunteers (IRB Approval No. IRB00006761-M2024690) at the Peking University Third Hospital. The experimental setup and instrumentation are shown in Fig. 1b and explained in the Method section. Arms, with strong scattering effects due to bone, pose a significant challenge for traditional solvers. However, S^2NO -FWI preserved accuracy and efficiency: leveraging multiple GPUs (one per slice), it reconstructed an 11-slice (5 cm) arm volume in 8.50 minutes, whereas frequency-domain FWI with conventional solvers took about 60 minutes per slice on the same hardware (Fig. 6c).

Figure 6a,d and Fig . 7a,c present 3D reconstructions of the arms from both female and male subjects obtained via various methods. The segmented and color-coded reconstructions demonstrate that the S^2NO -based inversion effectively restored arm anatomy by the distinct delineation of the skin, humerus, blood vessels (e.g., brachial and cephalic veins), and muscles (e.g., biceps brachii and triceps brachii). Moreover, distinct muscle–bone interfaces not only facilitate differentiation between male and female arms based on muscle ratios but also enable the extraction of muscle metrics such as cross-sectional area and volume, which may assist in the diagnosis of sarcopenia (29,30). Reference MRI images from the same subjects are provided as a gold-standard comparison.

Notably, S^2NO outperformed other methods, delivering high-resolution reconstructions with a parameter-free resolution of 1.09 mm, closely approaching the MRI standard of 0.88 mm. Sagittal and coronal cross-sectional reconstructions further demonstrate the consistent performance of S^2NO across different imaging planes. In contrast, the numerical solver, CBS, exhibited scattering artifacts near bone structures and distinct black-ring artifacts in arm reconstructions, indicating that traditional numerical solvers are less robust in strongly scattering samples and tend to overfit to observational noise. In comparison, the S^2NO -based approach demonstrated superior stability.

***In Vivo* 3D Human Legs**

Finally, we applied our method to high-resolution 3D USCT imaging of human legs—a challenging yet crucial task for diagnosing sports injuries (e.g., muscle strain, Achilles tendon rupture) and musculoskeletal conditions (e.g., age-related osteoporosis). Using S^2NO -FWI, we achieved high-fidelity 3D reconstructions closely matching reference MRI results (Fig. 6b,d and Fig. 7b,d). For two healthy volunteers (IRB Approval No. IRB00006761-M2024690), we reconstructed 11 mid-thigh slices spanning approximately 5 cm and combined them to yield a 3D sound speed model. Semantic segmentation of the reconstructed volumes (Fig. 6b and Fig. 7b) indicates that S^2NO accurately delineates skin, muscle (e.g., biceps femoris, gracilis, sartorius), fat, blood vessels (e.g., deep femoral vein, great saphenous vein), and femoral structures—including low-density marrow—with a parameter-free resolution of approximately 1.30 mm, an achievement unattainable using classical DAS. The strong scattering in musculoskeletal tissues results in observed signals with extremely low signal-to-noise ratios, complicating the accurate determination of first-arrival times and ultimately causing ToFT to fail in arm and leg imaging applications. Compared to traditional FWI, which required over 133 minutes (around 2.2 hours) for reconstruction per slice, S^2NO completed the imaging under 10 minutes using one NVIDIA A800-80GB GPU. Notably, S^2NO -FWI’s speedup over conventional FWI grows from about 6× for arm imaging to 14× for leg imaging, revealing its superior performance on stronger scattering PDEs. This enables the first successful 3D USCT-FWI imaging of human legs, underscoring the method’s strong potential for efficient clinical applications where timely diagnosis is critical.

Discussion

In this paper, we present a novel generative neural physics framework for 3D USCT imaging overcomes the challenges of complex wave–PDE inversion across large computational domains. First, we introduced a Reality-to-Simulation dataset generation method using generative AI and accurate instrument simulator, creating the largest anatomically- and physically-realistic wave imaging dataset to date. Second, we developed the Strong Scattering Neural Operator (S^2NO), an innovative physics-inspired neural operator architecture designed to model complex wave propagation in strongly scattering media. After trained on the extensive dataset derived from the Reality-to-Simulation stage, S^2NO established itself as an accurate, efficient and versatile wave simulator for a broad range of realistic human tissues, including bone. Finally, in the Simulation-to-Reality stage, we integrated S^2NO into an iterative optimization pipeline for FWI reconstruction. Our method significantly accelerates reconstruction speed—by an order of magnitude compared to conventional numerical solvers—while achieving MRI-comparable resolution. This computational efficiency, combined with the method’s robustness to complex scattering, enables rapid, high-resolution, *in vivo* USCT imaging of breast and 3D musculoskeletal tissues (e.g., arms and legs) for the first time, offering significant potential for clinical diagnosis and monitoring of tumor and muscle diseases.

Two key innovations drive the success of our framework. First, our cross-modality data generation—combining physics-based modality transfer from X-ray CT to ultrasound with diffusion-based image augmentation—enables highly realistic simulation of human organs under experimental USCT conditions, even when access to real-world USCT data is limited. This establishes a critical and reliable foundation for training and evaluating deep learning models. Second, our S^2NO -based iterative reconstruction addresses the inverse scattering problem (mapping observations to images: $y \rightarrow c$) by explicitly disentangling the forward wave physics $p(y|c)$ from image priors $p(c)$ through a Bayesian formulation, $p(c|y) \propto p(y|c)p(c)$. Unlike conventional direct inversion networks, which directly learn the posterior mapping $p(c|y)$, S^2NO robustly models the highly oscillatory wave phenomena inherent in USCT, $p(y|c)$ (Fig. 8). This approach emphasizes explicit modeling of wave physics rather than merely memorizing structural patterns, resulting in superior generalization to unseen tissues and imaging instruments, and positioning our method for broader clinical adoption.

Despite these advancements, our method has some limitations. It currently simplifies certain aspects of wave physics, considering only acoustic waves and neglecting elastic waves, which are sometimes crucial in bones (31). Additionally, attenuation effects are not modelled, and wave propagation is assumed to occur in a 2D plane, while real-world scenarios involve 3D propagation (32). These simplifications lead to discrepancies between our model and the actual physics of wave propagation in complex tissues. In future work, we aim to address these limitations by incorporating more accurate wave physics, including elasticity, attenuation, and full 3D propagation. Expanding the dataset to cover a wider range of organs and tissues, such as brain tissue and skull bone, will also be a priority. Additionally, as our framework is generalizable to all wave-based imaging problems, we plan to extend its application to other scientific domains, such as seismic imaging in geophysics and optical diffraction tomography in cell biology. By continuing to refine our method and broaden its applications, we believe our Real2Sim2Real framework, powered by generative AI and S^2NO , can significantly advance not only medical imaging but also various other fields that rely on wave-based imaging technologies.

Method

Generation of USCT Dataset with Realistic Anatomy and Experimental Scenario

To develop more effective neural networks for USCT FWI, we have created a USCT dataset featuring anatomically realistic phantoms and corresponding wavefields simulated using parameters from an actual USCT system. Our dataset comprises 22,047 digital human organ phantoms, including 7,520 breasts, 7,526 arms and 7,001 legs. For each phantom, we simulate wavefields from 64 different sources at 8 different frequencies, resulting in a total of 11,288,064 input-output data pairs. Our dataset is released at <https://open-waves-usct.github.io/>.

Physics-based Generation of Limited Amount of Organ Phantoms

Breasts: A specialized tool from the Virtual Imaging Clinical Trial for Regulatory Evaluation (VICTRE) initiative at the US Food and Drug Administration (US-FDA) enables the creation

of anatomically realistic, digital 3D breast models³³. This tool is capable of generating diverse tissue maps of breast anatomy. We follow the approach of Li et al (33) to build sound speed distributions based on different breast density types, including all-fatty (FAT), fibroglandular (FIB), heterogeneous (HET), and extremely dense (EXD) breasts. The breast data generation process consists of three steps:

1. The VICTRE tool are utilized to generate 3D breast models.
2. The 3D models are converted into 2D phantoms through a process of random slicing. Moreover, the 2D phantom slices are translated to the center of region and randomly scaled to increase diversity.
3. Distinct breast tissues (e.g., skin, adipose tissue, and muscle) are segmented and physically realistic sound speeds, each with small random perturbations, are assigned to the corresponding tissue regions. The region surrounding the breast models is then filled with water to replicate experimental conditions. We applied additional random rotations to the samples to enhance the authenticity of the data.

This methodology has enabled us to generate a comprehensive dataset of 3,520 anatomically realistic breast samples. However, due to the high computational cost of using VICTRE tools for generating 3D breast models, only a limited set of hyperparameters could be explored, restricting the diversity of the dataset.

Arms and Legs: Due to the lack of existing organ simulation tools for the arm and leg, we designed a pipeline to generate USCT sound speed models via physics-inspired style transfer from X-ray CT images. The X-ray CT data were collected at the Orthopedics Department of Peking University Third Hospital using clinical imaging equipment. We collected 3D arm scan data from 151 volunteers and 3D leg scan data from 41 additional volunteers, some of whom presented with fractures. All participants were recruited from the Orthopedic Department of Peking University Third Hospital, and informed consent was obtained prior to data collection. The *in vivo* study was approved by the Peking University Third Hospital Medical Science Research Ethics Committee (Project M2022262) and carried out in accordance with all relevant ethics standards. Selected slices from these 3D scans were used as the input, and anatomically accurate sound speed maps for the

arms and legs were generated using a style transfer approach inspired by physical modeling. This process also involves three steps:

1. We conduct semantic segmentation of X-ray CT images using the SAM vision foundational model.
2. Each segmented region is mapped to a sound speed range that aligns with physical reality.
3. The surrounding medium is assigned the sound speed of water. We applied additional random rotations to the samples to enhance the authenticity of the data.

Employing this method, we have effectively generated 809 sliced arm samples and 1,001 sliced leg samples. However, due to the structural similarity of leg cross-sections from the same individual, the resulting dataset exhibits limited diversity.

Fine-tuning Stable Diffusion for Data Augmentation

To address the limited diversity of the three organ phantoms, we propose a strategy that augments experimental data by fine-tuning a pretrained image generative model. Specifically, for each organ type, we select a subset of 2D phantom slices and fine-tune a text-to-image Stable Diffusion model using the DreamBooth (34) method to produce additional slices. This approach comprises three major steps:

1. For each organ, we fine-tune the Stable Diffusion model with the prompt: “Grayscale image of a cross-section of a breast/arm/leg phantom”.
2. Generate images from the fine-tuned model using the same prompt and filter out implausible outputs according to physical principles.
3. Perform post-processing to align the generated images with the physics-based phantoms.

Using this approach, we produced 4,000 breast, 6,717 arm, and 6,000 leg phantoms. These high-quality samples were subsequently used to generate sound speed–wavefield pairs for training neural surrogates.

Wavefield Simulation using Experimental USCT Settings

Wavefields in our dataset were simulated using the experimental parameters of two actual annular USCT systems. Specifically, the breast dataset employed the system configuration described by Ali et al (3), whereas the arm and leg datasets utilized a system of similar size but with a distinct transducer arrangement. Both USCT system comprise 256 transducers uniformly distributed around a ring with a diameter of around 22 centimeters. The system operates within a frequency range of 0.25 MHz to 1.2 MHz, corresponding to approximate acoustic wavelength of 1 mm to 5 mm. In our simulations, we focus on wave propagation at discrete frequencies of 0.25, 0.3, 0.35, 0.4, 0.45, 0.5, 0.55, and 0.6 MHz, yielding approximately 40 to 100 wavenumbers within the field of view. For each phantom, we simulated 64 wavefields corresponding to distinct point sources, uniformly selected from the 256 transducers by employing every fourth transducer as the source location. The numerical solutions of Helmholtz equations are simulated with the CBS (20) algorithm.

Strong Scattering Neural Operator (S^2NO) and S^2NO -based FWI

The S^2NO serves as a proficient tool designed to accurately and efficiently approximate the implicit mapping $f_{c,\rho} : c, \rho \rightarrow u$ as defined by the Helmholtz equation. Drawing inspiration from the CBS solver for the Helmholtz equation, the S^2NO utilizes an iterative scheme in developing its neural network architecture. Moreover, the inputs and outputs within each iterative block of the S^2NO are carefully designed based on physical concepts, thereby enhancing the operator's ability to approximate and generalize effectively.

Born Series and Convergent Born Series

By defining a scattering potential $v = \left(\frac{\omega}{c(x)}\right)^2 - \kappa^2 - i\varepsilon$, with $\kappa^2, \varepsilon > 0$, we can reformulate the Helmholtz equation as

$$\mathcal{S}'u(x) \triangleq [\nabla^2 + \kappa^2 + i\varepsilon] u(x) = -\rho(x) - v(x)u(x). \quad (2)$$

This leads to the derivation of the Born series for the Helmholtz equation:

$$u = \mathcal{G}\rho + \mathcal{G}v u \Rightarrow u = \sum_{n=0}^{\infty} (\mathcal{G}v)^n \mathcal{G}\rho. \quad (3)$$

where $\mathcal{G} = \mathcal{F}^{-1} \circ (p^2 - \kappa^2 - i\varepsilon)^{-1} \circ \mathcal{F}$ is the Green operator of $\mathcal{S}'(\cdot) = [\nabla^2 + \kappa^2 + i\varepsilon](\cdot)$, \mathcal{F} is the Fourier transform operator, and $p^2 = p_x^2 + p_y^2$ is the squared magnitude of the Fourier-transformed coordinates. This series solution can also be used to derive an iterative form of the solution

$$\begin{cases} u_{n+1} &= u_0 + (\mathcal{G}v) u_n, \\ u_0 &= \mathcal{G}\rho. \end{cases} \quad (4)$$

While the Born series has been effective for solving Helmholtz equations with weak scattering potentials, its convergence is limited in the presence of strongly scattering samples. This poses challenges for practical wave simulations, including biomedical USCT.

To address this limitation, Osnabrugge et al. (20) proposed a modification to the Born series by introducing a preconditioner $q = 1 - \frac{i\nu}{\varepsilon}$. This approach involves multiplying both sides with $1 - q$ and introducing a new operator $\mathcal{M} = (1 - q) \mathcal{G}v + q$, leading to a new formulation

$$(1 - q)u = (1 - q) \mathcal{G}\rho + (1 - q) \mathcal{G}vu \Rightarrow u = \sum_{n=0}^{\infty} (\mathcal{M})^n ((1 - q) \mathcal{G}\rho). \quad (5)$$

whose iterative scheme writes

$$\begin{cases} u_{n+1} &= u_0 + \mathcal{M} u_n, \\ u_0 &= (1 - q) \mathcal{G}\rho. \end{cases} \quad (6)$$

Here, the operator \mathcal{M} maintains a spectral radius smaller than 1 with a suitable choice of ε and κ , ensuring convergence for strong scattering potentials.

S^2NO Architecture

The S^2NO 's network architecture is crafted based on the iterative structure of the CBS. As depicted in Fig. 3a, S^2NO comprises three distinct phases: 1) encoding the sound speed c and the source ρ into a latent space to obtain the representations of q , v and u_0 ; 2) iteratively updating the latent wavefield states u_n using S^2NO layers; and 3) projecting the final latent state back into the physical space. This architecture is mathematically represented as follows:

$$\begin{aligned} \text{Phase 1: } & q = \mathcal{E}_{\theta_q}(c), \quad v = \mathcal{E}_{\theta_v}(c), \quad u_0 = \mathcal{E}_{\theta_{\text{init}}}(c, \rho), \\ \text{Phase 2: } & u_{n+1} = \mathcal{M}_{\theta_M}(u_n, q, v) + u_0, \quad n = 1, \dots, N, \\ \text{Phase 3: } & u_{\text{out}} = \mathcal{D}_{\theta_{\text{pred}}}(u_N). \end{aligned} \quad (7)$$

In this model, q and v are the latent states of the preconditioner and the scattering potential, u_n is the latent state of the wavefield, and u_{out} is the output wavefield in the physical space. The encoders \mathcal{E}_{θ_q} , \mathcal{E}_{θ_v} and $\mathcal{E}_{\theta_{\text{init}}}$ process the auxiliary variables of the preconditioner, the scattering potential and the initial wavefield, respectively, while \mathcal{M}_{θ_M} acts as the operator \mathcal{M} to update the latent wavefield. Indeed, we replace the Green operator \mathcal{G} in \mathcal{M} with a spectral convolution layer, obtaining the S^2NO layer \mathcal{M}_{θ_M} :

$$\mathcal{M}_{\theta_M}(u_n, q, v) = \Phi_{\theta_M} \left((1 - q) \mathcal{F}^{-1} \circ R_{\theta_M} \circ \mathcal{F}(u_n v) + q u_n \right). \quad (8)$$

Here, Φ_{θ_M} is a CNN module and R_{θ_M} represents the trainable Fourier modes (21). Each S^2NO layer uses independent parameters to boost the network's representational capacity. The decoder $\mathcal{D}_{\theta_{\text{pred}}}$ then predicts the wavefield in physical space. The details of implementation and training process are provided in Supplementary Note 3. By explicitly embedding physical laws into the architecture, S^2NO demonstrates superior generalization capabilities on unseen sound speed models and sources (see Supplementary Tables S6-S8).

S^2NO -based FWI

The PDE constrained optimization problem defined by Equation (x) is typically addressed with gradient-based optimizers, where the adjoint method is a common approach for computing the gradient. Using the method of Lagrange multipliers, the constrained optimization problem can be reformulated as an unconstrained form:

$$\min_{c, u_k, \lambda} \mathcal{L} = \sum_{k=1}^K \mathcal{L}_k = \sum_{k=1}^K \|y_k - u_k(x_f)\|_2^2 - \sum_{k=1}^K \left\langle \lambda_k(x), \left[\nabla^2 + \left(\frac{\omega}{c(x)} \right)^2 \right] u_k(x) + \rho_k(x) \right\rangle. \quad (9)$$

where \mathcal{L} is the Lagrangian function, $\langle f, g \rangle$ denotes the real part of inner product of functions f and g in $L^2(\mathbb{C})$. The gradient $\frac{\partial \mathcal{L}_k}{\partial c}(x)$ is proportional to the product of u_k and λ_k :

$$\frac{\partial \mathcal{L}_k}{\partial c}(x) = -2\omega^2 \text{Re} \left(\frac{\lambda_k^*(x) u_k(x)}{c(x)^3} \right), \quad (10)$$

where the wavefield u_k and the adjoint state λ_k are obtained by solving the Helmholtz equation

$$\begin{cases} \left[\nabla^2 + \left(\frac{\omega}{c(x)} \right)^2 \right] u_k(x) = -\rho_k(x), \\ \left[\nabla^2 + \left(\frac{\omega}{c(x)} \right)^2 \right] \lambda_k(x) = 2 \sum_{i=1}^K \left[u_k(x_f^{(i)}) - y_k^{(i)} \right] \delta(x_f^{(i)}). \end{cases} \quad (11)$$

By incorporating S^2NO as an approximation of the solution maps $f_{c,\rho}(c(x), \rho(x)) \rightarrow u(x)$, Equation (x) can be approximated by

$$\begin{cases} u_k(x) = S^2NO(c(x), \rho_k(x)), \\ \lambda_k(x) = S^2NO\left(c(x), -\sum_{i=1}^K \left[u_k(x_f^{(i)}) - y_k^{(i)} \right] \delta(x_f^{(i)}) \right). \end{cases} \quad (11)$$

Finally, the optimization problem is solved iteratively using gradient-based optimization methods (e.g., L-BFGS, NCG).

Experimental Settings of *in vivo* Human Arms and Legs Data Acquisition

Annular-array USCT System

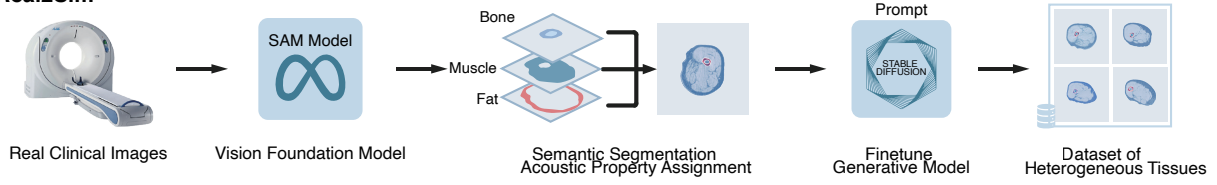
in vivo USCT data acquisition for human arms and legs was performed using a circular transducer array. Axial scanning was achieved by elevating the instrument with retractable bellows, enabling layer-by-layer measurements. In this annular-array USCT system, each transducer element functions as a small planar source rather than a true point source, resulting in a directivity effect that confines wave propagation largely within a 2D slice. Consequently, 2D modeling effectively captures the key imaging characteristics of USCT. The system consists of 256 transducers arranged in a circular geometry surrounding the region of interest. Each transducer operates both as transmitter and receiver. During data collection, one transducer emits an acoustic signal while all 256 transducers act as receivers. This process is repeated for all 256 elements, resulting in a full set of measurements for each layer. By vertically scanning the arm or leg in steps, multiple 2D slices are acquired, which are then stacked to reconstruct a full 3D volume. The transducers have a center frequency of 0.9 MHz. To enhance low-frequency information capture, a square wave signal pulse with a carrier frequency of 0.6 MHz and a transmission voltage of 90 V is used. Signals are sampled at 25 MHz over a duration of 198 μs . The acquired signals are in the time domain. To facilitate frequency-domain full waveform inversion and improve the signal-to-noise ratio, a Butterworth bandpass filter is used to filter the acquired signals. The filtered time-domain signals are then converted into multiple single-frequency components via discrete Fourier transform. The *in vivo* USCT experiments on the arm and leg were conducted on two adult volunteers (one male and one female) for whom informed consent was obtained prior to the experiment. The study protocol was approved

by the Peking University Third Hospital Medical Science Research Ethics Committee (Project ID: IRB00006761-M2024690) and was conducted in accordance with all relevant ethical regulations.

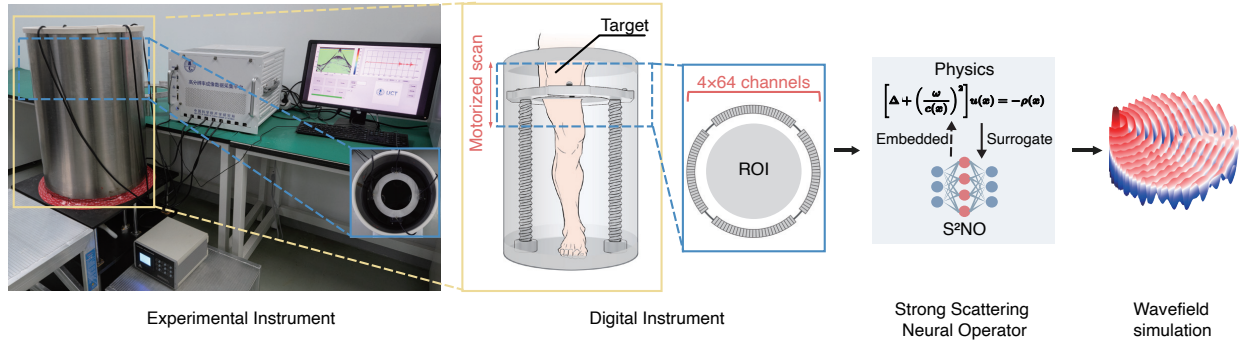
3T MRI Acquisition

A GE Discovery MR750W 3.0T MRI scanner equipped with an 8-channel PA Matrix coil was used for performing the bilateral thigh MR scans. Participants were positioned supine, feet first, with the long axis of the lower limbs aligned with the scanner's main axis. The coil was positioned to fully cover the patella for axial imaging. Scanning protocols included: axial fat-suppressed T2-weighted imaging (repetition time (TR) = 5169 ms and echo time (TE) = 72.1 ms) and axial T1-weighted imaging (TR = 618 ms, TE = 11.1 ms, FOV = $400 \times 275.2 \text{ mm}^2$, slice thickness = 6 mm, inter-slice gap = 0.6 mm, matrix = 320×256).

a Real2Sim



b Build Digital Simulator



c Sim2Real

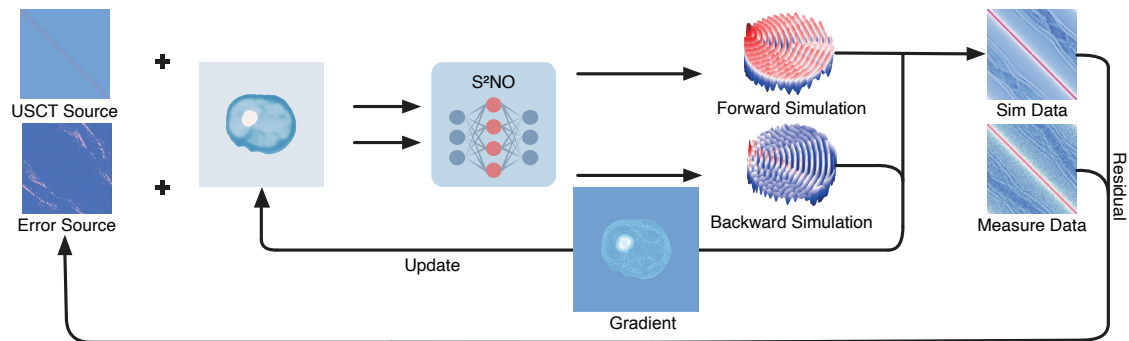


Figure 1. Schematic illustration of the proposed generative neural physics framework. (A)

Clinical images from alternative imaging modalities (e.g., X-ray CT) are segmented using the Segment Anything Model (SAM), and then converted into sound speed maps according to known tissue acoustic properties. These maps fine-tune a pretrained generative model to produce a diverse library of heterogeneous tissue phantoms. **(B)** An annular transducer array with motorized retractable bellows is employed to acquire slice-wise USCT data. A high-fidelity numerical solver simulates the corresponding acoustic wavefields for each tissue phantom under realistic experimental scenarios, producing paired data to train the Strong Scattering Neural Operator (S^2NO) as an efficient digital instrument simulator. **(C)** The trained S^2NO is deployed as a forward surrogate in USCT imaging to solve a full waveform inversion problem. It generates scattered wavefields from the estimated sound speed model, and the residuals between simulated and measured data at sensor positions are backpropagated to iteratively update the model via gradient-based optimization.

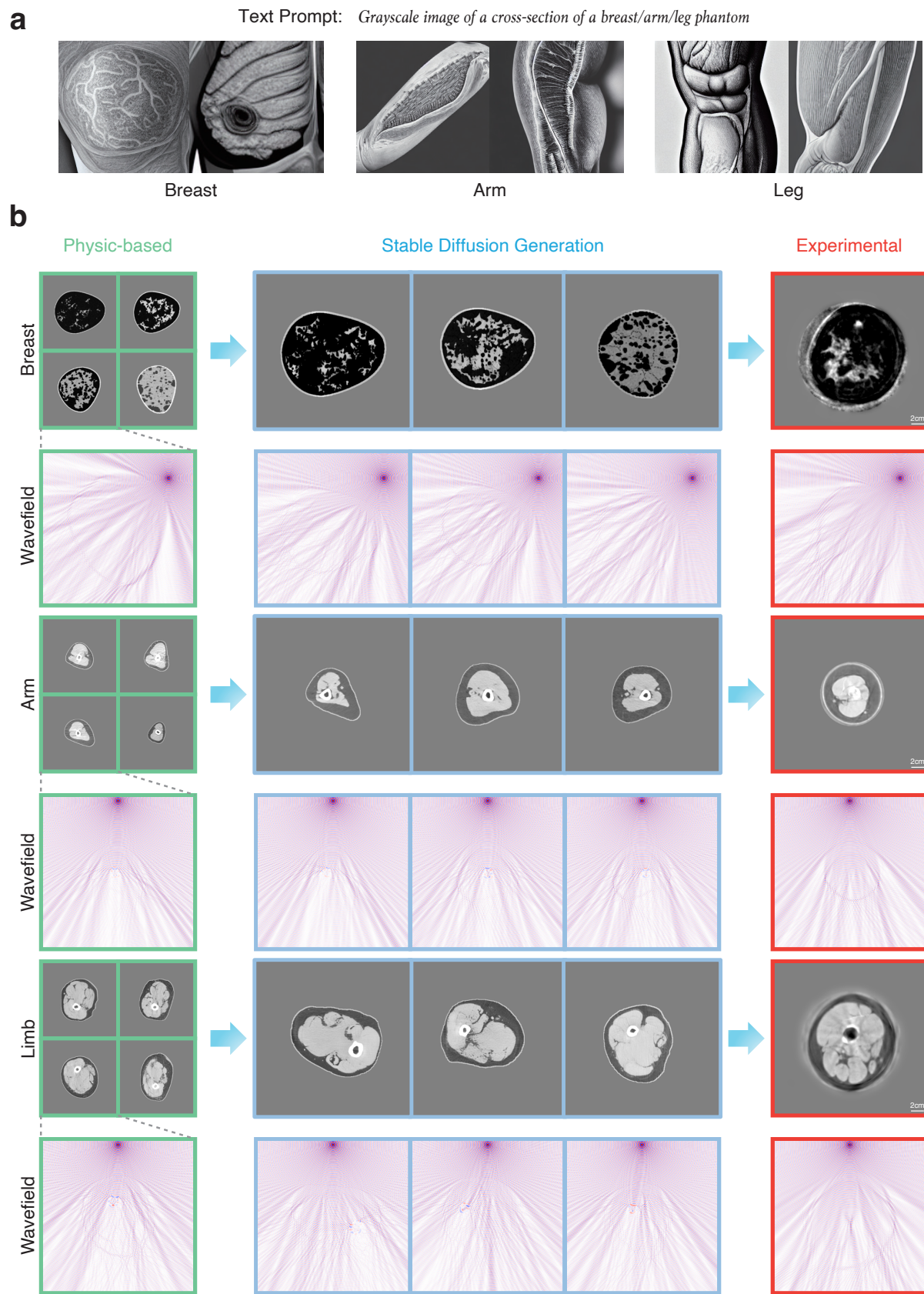


Figure 2. Comparison of synthetic phantoms and *in vivo* human tissues. (A) A base Stable Diffusion model produces phantoms with the semantically meaningful morphology but lacks realistic anatomical details. (B) After fine-tuning on a limited set of physics-based phantoms created via style transfer from cross-modality medical images, the model produces sound-speed maps of breast, arm, and leg tissues that closely match *in vivo* measurements.

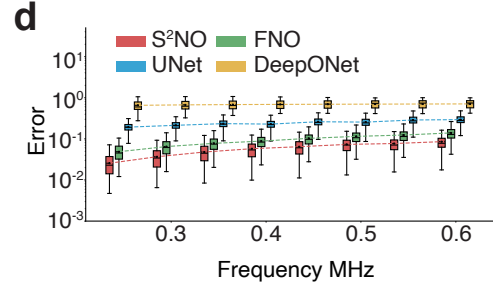
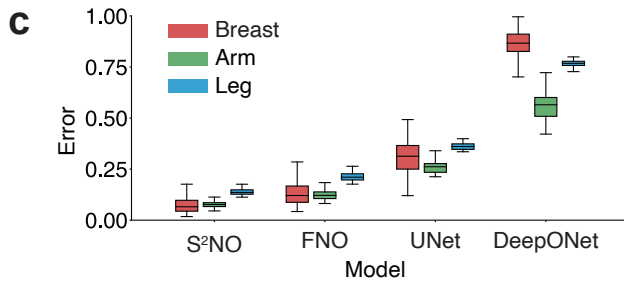
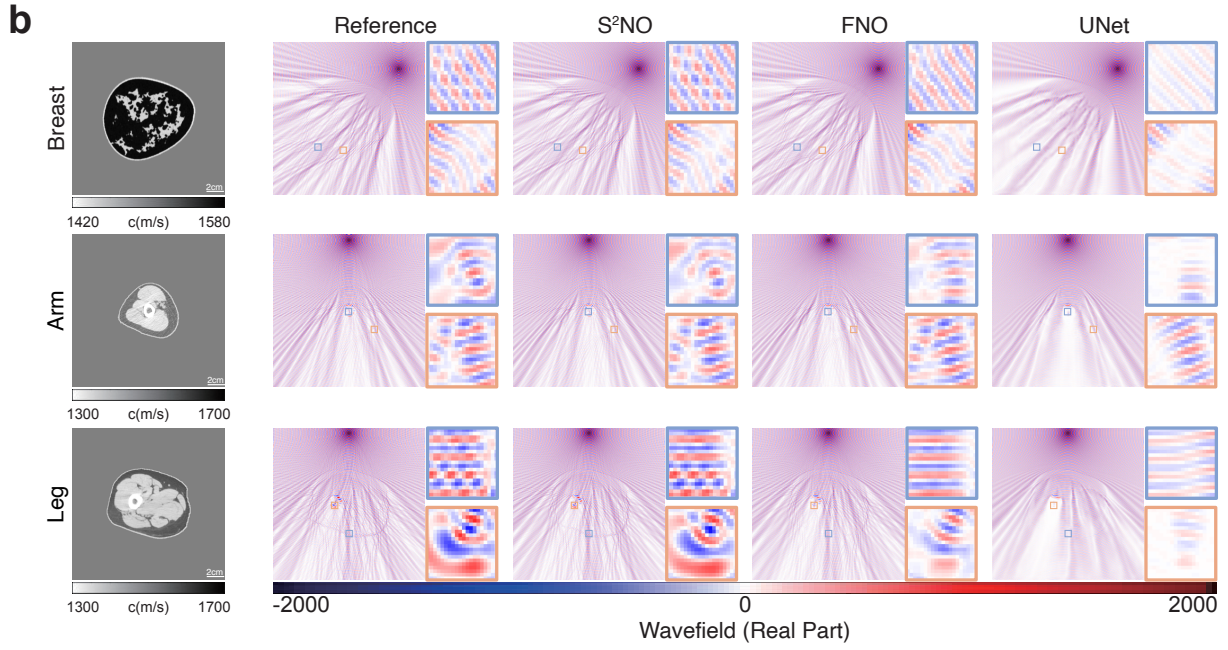
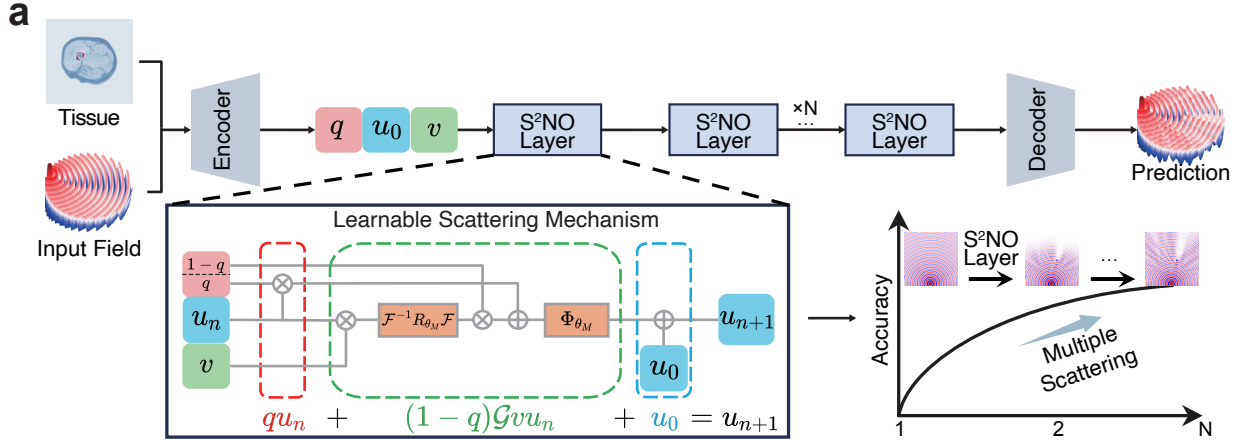


Figure 3. The architecture and forward simulation result of S^2NO . (A) Schematic overview of the entire S^2NO architecture. The sound speed and incident field are encoded into a latent space as three auxiliary variables representing the wavefield (u), scattering potential (v) and preconditioner (q). Within the latent space, the wavefield is iteratively updated using a learnable scattering mechanism, where each iteration corresponds to an S^2NO layer. A decoder then projects the latent variables to the physical space to produce the predicted wavefield. (B) Wavefield predictions from S^2NO and baseline models for breast, arm, and leg phantoms at 0.6MHz. S^2NO accurately captures complex scattering patterns, particularly at the marrow cavity and the skin-air interface. (C) Forward simulation errors of S^2NO and baseline models for breast, arm, and leg phantoms at a 0.6MHz setting. Boxplots show the median (central line) and interquartile range (IQR, box); whiskers extend to the smallest and largest values within $1.5 \times$ the IQR (outliers omitted), sample size $N=320/373/108$ for Breast/Arm/Leg dataset. (D) Comparison of forward simulation errors between S^2NO and the baseline models for all organ phantoms at frequencies of 0.25 0.6 MHz. The setting of the boxplots is the same as (C), sample size $N=801$. Despite the increased challenge at higher frequencies, S^2NO consistently outperforms all baseline methods at every frequency and for every organ.

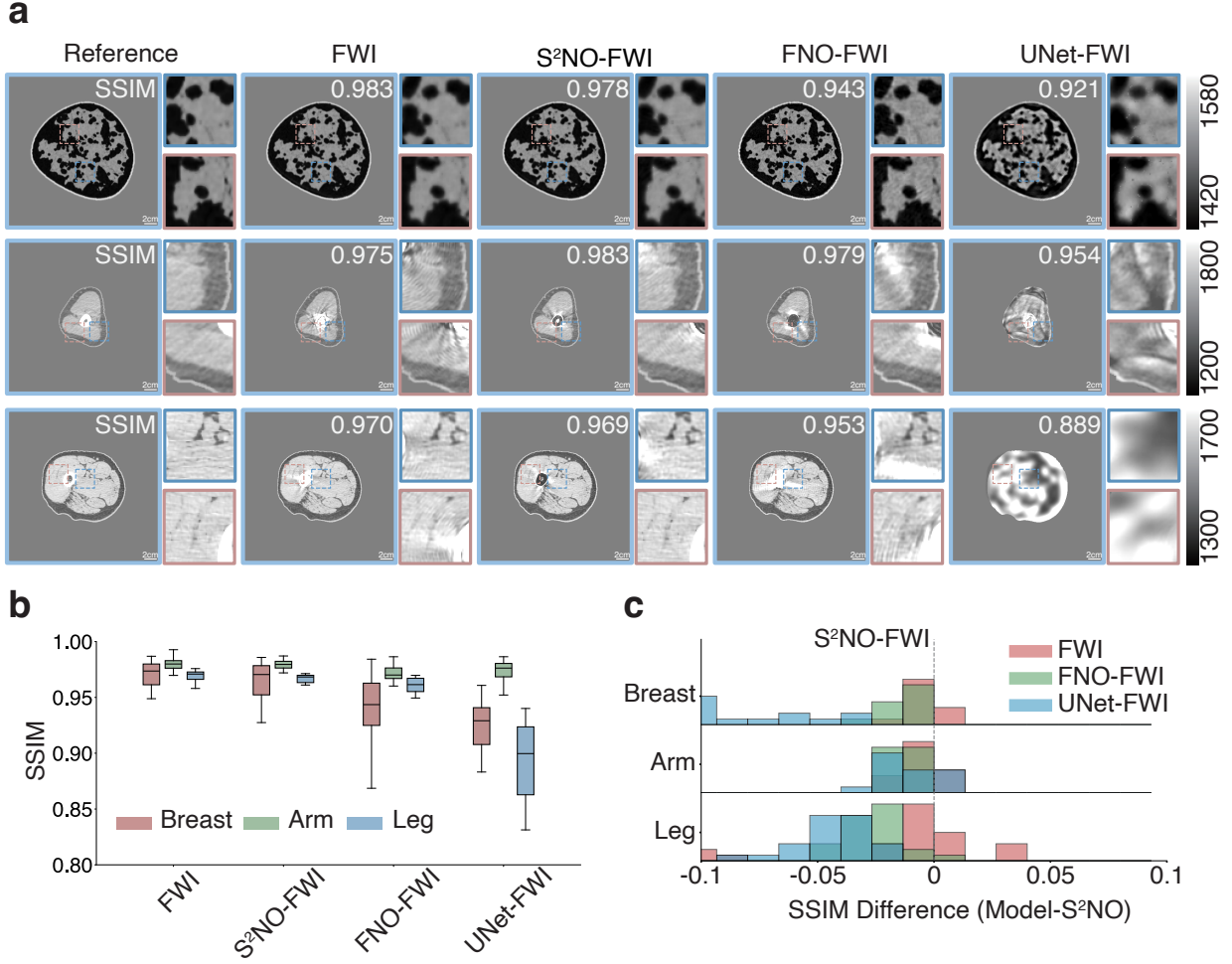


Figure 4. The Inversion results of synthetic breast, arm and leg phantoms. (A) Comparison between the reference breast, arm and leg phantoms and the reconstructed phantoms using different model (numerical solver, S^2NO , FNO and UNet). **(B)** Statistical summary of SSIM values for reconstruction results of breast, arm, and leg phantom in test dataset using various models (numerical solver, S^2NO , FNO and UNet). Boxplots show the median (central line) and interquartile range (IQR, box); whiskers extend to the smallest and largest values within $1.5\times$ the IQR (outliers omitted), sample size $N=24/16/12$ for Breast/Arm/Leg dataset. **(C)** Distribution of SSIM differences between S^2NO and other methods computed on a sample-by-sample basis. S^2NO matches the imaging quality of conventional numerical solver while outperforming all other baseline approaches.

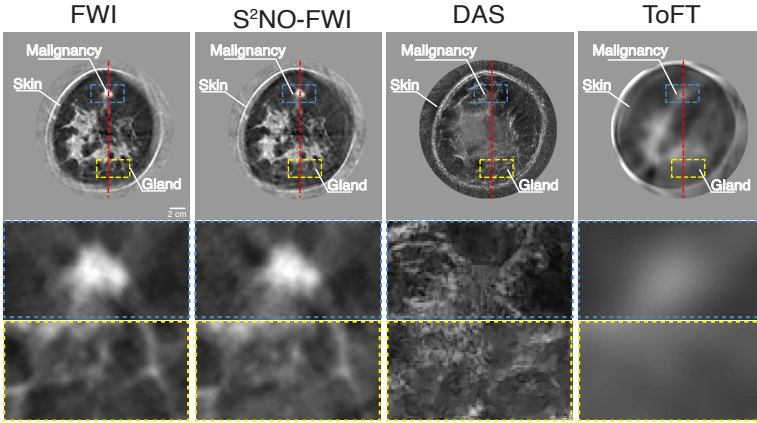
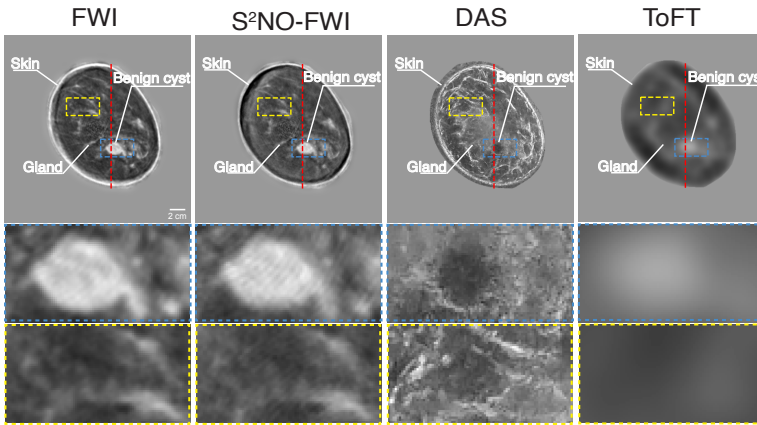
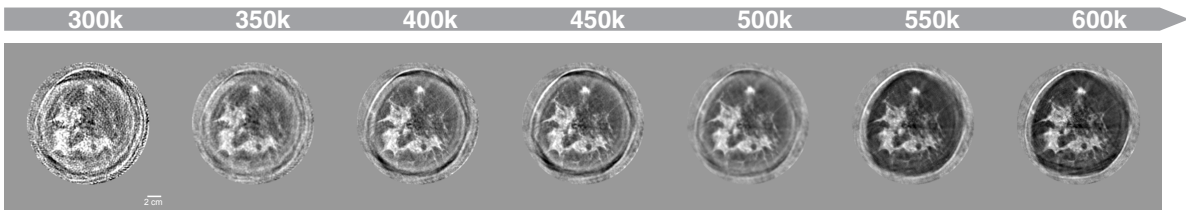
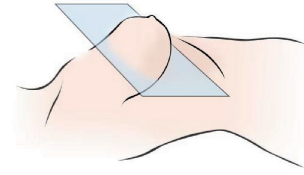
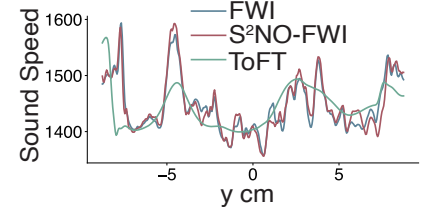
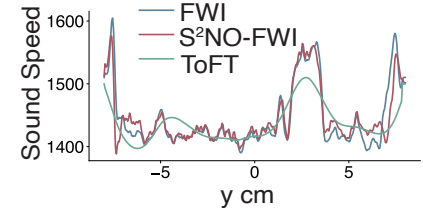
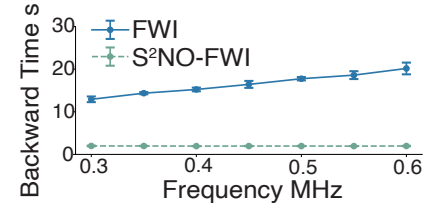
a**b****c****d****e****f****g**

Figure 5. The USCT imaging of two breasts with malignancy or benign cyst. (A-B)

Comparison of reconstructions of breasts with a spiculated malignancy (A) and a benign cyst (B), obtained using various imaging techniques (FWI, S^2NO -FWI, ToFT, and DAS). S^2NO -FWI provides image quality comparable to traditional FWI solvers, particularly in resolving critical structures such as tumors and glandular tissue, whereas DAS and ToFT fail to reconstruct meaningful internal anatomy. (C) Reconstruction accuracy of S^2NO -FWI improves progressively with increasing dataset bandwidth. (D) Schematic illustration of cross-sectional data acquisition for breast imaging. (E-F) One-dimensional velocity profiles extracted at specific positions (red line) from the reconstructed breast model with a spiculated malignancy (E) and a benign cyst (F). (G) Computational time per iteration for traditional solver-based FWI and S^2NO -FWI across varying frequencies. S^2NO accelerates computations by over tenfold. The data points denote mean values, and the vertical bars indicate the standard deviation, sample size $N=10$.

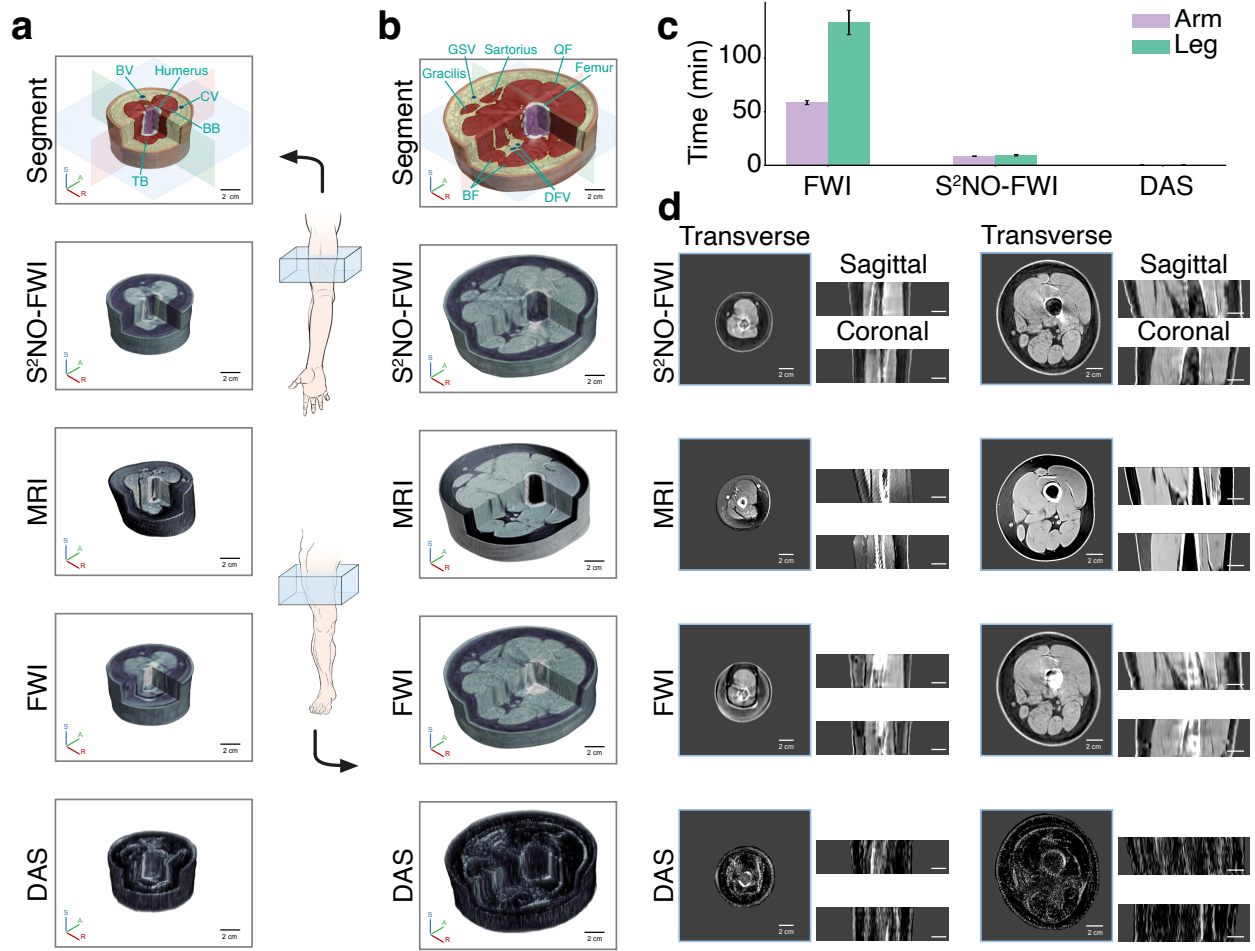


Figure 6. The 3D USCT imaging of a female's leg and arm. (A-B) 3D reconstructions of the female arm (A) and leg (B) were obtained by S^2NO -FWI, MRI, traditional FWI and DAS, and assembled from 11 segmented slices. The color-coded segmentations of S^2NO -FWI reconstruction are shown for both models. S^2NO -FWI outperforms DAS and traditional FWI, delivering high-resolution 3D USCT reconstructions with MRI comparable image quality. (C) A comparison of computational times across inversion methods reveals that S^2NO achieves at least a fourteen-fold acceleration. The bars represent the mean \pm standard deviation, sample size N=11. (D) Representative transverse, sagittal and coronal sections obtained by S^2NO -FWI, MRI, FWI and DAS demonstrate that S^2NO maintains consistent accuracy across all orientations. BF, biceps femoris; QF, quadriceps femoris; DFV, deep femoral vein; GSV, great saphenous vein; BB, biceps brachii; TB, triceps brachii; BV, brachial vein; CV, cephalic vein.

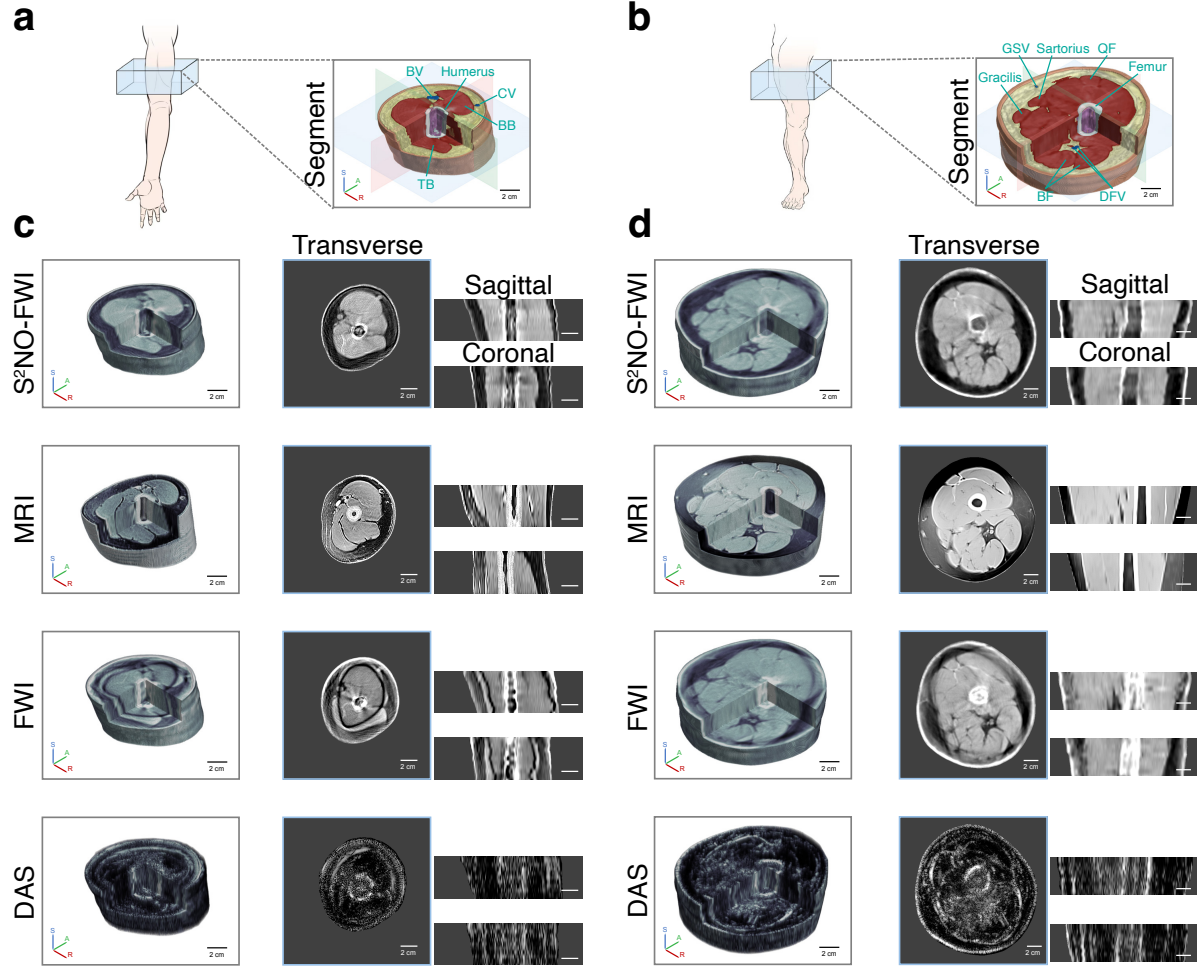


Figure 7. The 3D USCT imaging of a male's leg and arm. (A-B) The color-coded segmentations of S^2NO -based FWI reconstruction results are shown for 3D arm (A) and leg (B). (C) 3D reconstructions of the male arm, obtained by S^2NO -based FWI, MRI, traditional FWI and DAS, were assembled from 11 segmented slices. Representative transverse, sagittal and coronal sections obtained by different imaging methods are also provided. (D) 3D reconstructions of the male leg, obtained by S^2NO -based FWI, MRI, traditional FWI and DAS, were assembled from 11 segmented slices. BF, biceps femoris; QF, quadriceps femoris; DFV, deep femoral vein; GSV, great saphenous vein; BB, biceps brachii; TB, triceps brachii; BV, brachial vein; CV, cephalic vein.

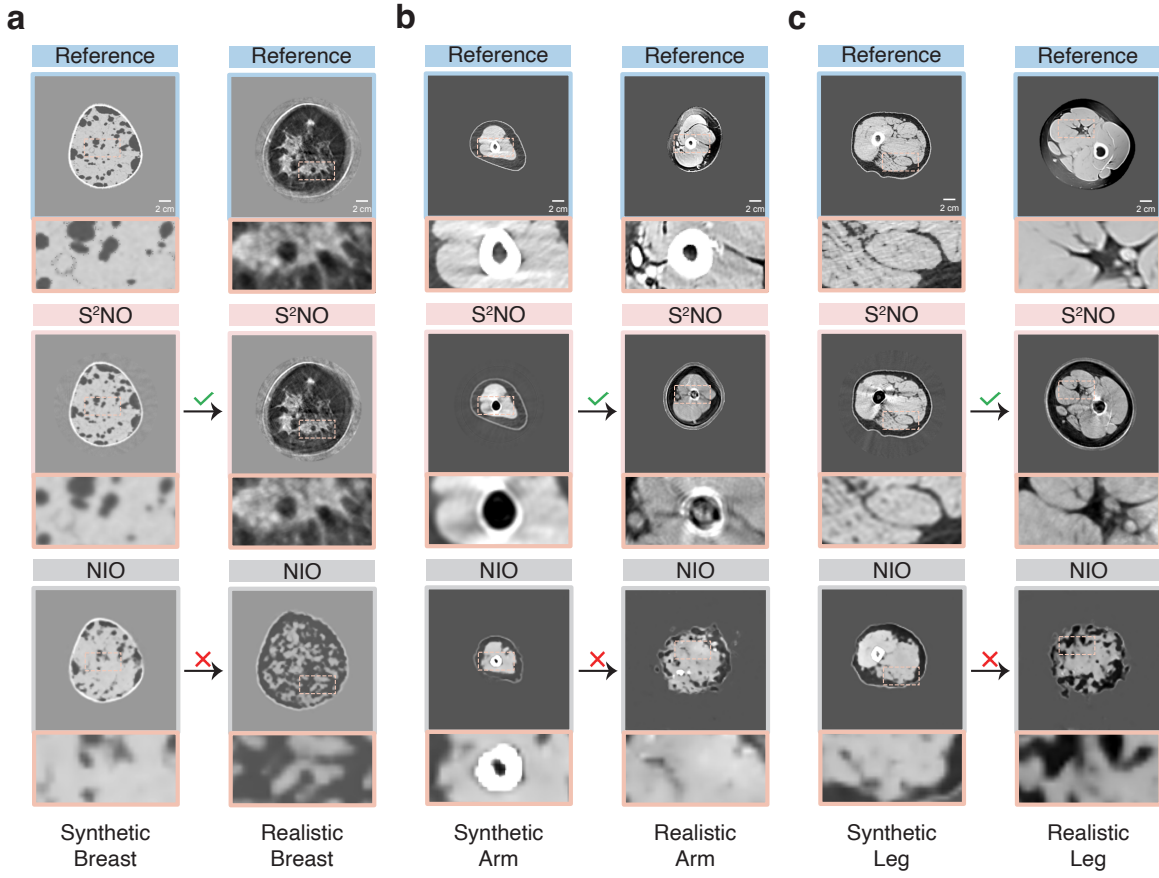


Figure 8. Comparison of reconstruction quality of synthetic phantoms and *in vivo* tissues between S^2NO and direct inversion method, Neural Inverse Operator (NIO). (A) The imaging results of synthetic breast phantom and *in vivo* breast using both S^2NO -FWI and NIO. The numerical solver-based FWI reconstruction is provided as reference. (B) The imaging results of synthetic arm phantom and *in vivo* human arm using both S^2NO -FWI and NIO. The MRI imaging result is provided as reference. (C) The imaging results of synthetic leg phantom and *in vivo* human leg using both S^2NO -FWI and NIO. The MRI imaging result is provided as reference.

References and Notes

1. C. Rumack, D. Levine, Diagnostic ultrasound: diagnostic ultrasound (2017).
2. C. Cueto, *et al.*, Spatial response identification enables robust experimental ultrasound computed tomography. *IEEE Transactions on Ultrasonics, Ferroelectrics, and Frequency Control* **69** (1), 27–37 (2021).
3. R. Ali, *et al.*, 2-D slicewise waveform inversion of sound speed and acoustic attenuation for ring array ultrasound tomography based on a block LU solver. *IEEE transactions on medical imaging* **43** (8), 2988–3000 (2024).
4. C. Li, N. Duric, P. Littrup, L. Huang, In vivo breast sound-speed imaging with ultrasound tomography. *Ultrasound in medicine & biology* **35** (10), 1615–1628 (2009).
5. N. Ozmen, *et al.*, Comparing different ultrasound imaging methods for breast cancer detection. *IEEE transactions on ultrasonics, ferroelectrics, and frequency control* **62** (4), 637–646 (2015).
6. L. Guasch, O. Calderón Agudo, M.-X. Tang, P. Nachev, M. Warner, Full-waveform inversion imaging of the human brain. *NPJ digital medicine* **3** (1), 28 (2020).
7. A. Tarantola, Inversion of seismic reflection data in the acoustic approximation. *Geophysics* **49** (8), 1259–1266 (1984).
8. O. G. Ernst, M. J. Gander, Why it is difficult to solve Helmholtz problems with classical iterative methods. *Numerical analysis of multiscale problems* pp. 325–363 (2011).
9. Y. Fan, H. Wang, H. Gemmeke, T. Hopp, J. Hesser, Model-data-driven image reconstruction with neural networks for ultrasound computed tomography breast imaging. *Neurocomputing* **467**, 10–21 (2022).
10. L. Lozenski, *et al.*, Learned full waveform inversion incorporating task information for ultrasound computed tomography. *IEEE Transactions on Computational Imaging* **10**, 69–82 (2024).

11. R. Molinaro, Y. Yang, B. Engquist, S. Mishra, Neural inverse operators for solving PDE inverse problems. *arXiv preprint arXiv:2301.11167* (2023).
12. J. Ren, *et al.*, Deep learning with physics-embedded neural network for full waveform ultrasonic brain imaging. *IEEE transactions on medical imaging* **43** (6), 2332–2346 (2024).
13. P. Jin, *et al.*, An empirical study of large-scale data-driven full waveform inversion. *Scientific Reports* **14** (1), 20034 (2024).
14. N. McGreivy, A. Hakim, Weak baselines and reporting biases lead to overoptimism in machine learning for fluid-related partial differential equations. *Nature machine intelligence* **6** (10), 1256–1269 (2024).
15. G. E. Karniadakis, *et al.*, Physics-informed machine learning. *Nature Reviews Physics* **3** (6), 422–440 (2021).
16. M. Raissi, P. Perdikaris, G. E. Karniadakis, Physics-informed neural networks: A deep learning framework for solving forward and inverse problems involving nonlinear partial differential equations. *Journal of Computational physics* **378**, 686–707 (2019).
17. S. Wang, X. Yu, P. Perdikaris, When and why PINNs fail to train: A neural tangent kernel perspective. *Journal of Computational Physics* **449**, 110768 (2022).
18. A. Kirillov, *et al.*, Segment anything, in *Proceedings of the IEEE/CVF international conference on computer vision* (2023), pp. 4015–4026.
19. R. Rombach, A. Blattmann, D. Lorenz, P. Esser, B. Ommer, High-resolution image synthesis with latent diffusion models, in *Proceedings of the IEEE/CVF conference on computer vision and pattern recognition* (2022), pp. 10684–10695.
20. G. Osnabrugge, S. Leedumrongwatthanakun, I. M. Vellekoop, A convergent Born series for solving the inhomogeneous Helmholtz equation in arbitrarily large media. *Journal of computational physics* **322**, 113–124 (2016).
21. Z. Li, *et al.*, Fourier Neural Operator for Parametric Partial Differential Equations, in *International Conference on Learning Representations*.

22. L. Lu, P. Jin, G. Pang, Z. Zhang, G. E. Karniadakis, Learning nonlinear operators via DeepONet based on the universal approximation theorem of operators. *Nature machine intelligence* **3** (3), 218–229 (2021).
23. O. Ronneberger, P. Fischer, T. Brox, U-net: Convolutional networks for biomedical image segmentation, in *International Conference on Medical image computing and computer-assisted intervention* (Springer) (2015), pp. 234–241.
24. C. Bunks, F. M. Saleck, S. Zaleski, G. Chavent, Multiscale seismic waveform inversion. *Geophysics* **60** (5), 1457–1473 (1995).
25. M. Karaman, P.-C. Li, M. O’Donnell, Synthetic aperture imaging for small scale systems. *IEEE transactions on ultrasonics, ferroelectrics, and frequency control* **42** (3), 429–442 (1995).
26. K. E. Thomenius, Evolution of ultrasound beamformers, in *1996 IEEE Ultrasonics Symposium. Proceedings* (IEEE), vol. 2 (1996), pp. 1615–1622.
27. N. Duric, *et al.*, Detection of breast cancer with ultrasound tomography: First results with the Computed Ultrasound Risk Evaluation (CURE) prototype. *Medical physics* **34** (2), 773–785 (2007).
28. A. Descloux, K. S. Größmayer, A. Radenovic, Parameter-free image resolution estimation based on decorrelation analysis. *Nature methods* **16** (9), 918–924 (2019).
29. H. J. Stringer, D. Wilson, The role of ultrasound as a diagnostic tool for sarcopenia. *The Journal of frailty & aging* **7** (4), 258–261 (2018).
30. A. S. Tagliafico, B. Bignotti, L. Torri, F. Rossi, Sarcopenia: how to measure, when and why. *La radiologia medica* **127** (3), 228–237 (2022).
31. D. Komatitsch, C. Barnes, J. Tromp, Wave propagation near a fluid-solid interface: A spectral-element approach. *Geophysics* **65** (2), 623–631 (2000).
32. F. Lucka, M. Pérez-Liva, B. E. Treeby, B. T. Cox, High resolution 3D ultrasonic breast imaging by time-domain full waveform inversion. *Inverse Problems* **38** (2), 025008 (2022).

33. F. Li, U. Villa, S. Park, M. A. Anastasio, 3-D stochastic numerical breast phantoms for enabling virtual imaging trials of ultrasound computed tomography. *IEEE transactions on ultrasonics, ferroelectrics, and frequency control* **69** (1), 135–146 (2021).
34. N. Ruiz, *et al.*, Dreambooth: Fine tuning text-to-image diffusion models for subject-driven generation, in *Proceedings of the IEEE/CVF conference on computer vision and pattern recognition* (2023), pp. 22500–22510.
35. V. Perrot, M. Polichetti, F. Varray, D. Garcia, So you think you can DAS? A viewpoint on delay-and-sum beamforming. *Ultrasonics* **111**, 106309 (2021).
36. E. Zhang, *et al.*, Blending neural operators and relaxation methods in PDE numerical solvers. *Nature Machine Intelligence* **6** (11), 1303–1313 (2024).

Acknowledgments

Funding: This work was supported by the National Key R&D Program of China (No. 2022YFC3401100) (to Y.Z., Q.W, H.H, H.S), the National Natural Science Foundation of China (No. 92370125) (to Z.Z., Z.S), the Joint Research Project of the Shijiazhuang-Peking University Cooperation Program (to Z.H, H.S.), the National Natural Science Foundation of China (No. 12474461)(to Y.L¹, Y.L²), the Basic and Frontier Exploration Project Independently Deployed by Institute of Acoustics, Chinese Academy of Sciences (No. JCQY202402)(to C.S, W.L, Y.L²).(Y.L¹: Yang Lv; Y.L²: Yubing Li.)

Author contributions: Z.Z, Y.Z, C.S, Q.W, W.L, Y.L² and H.S conceived and designed the experiments. Z.Z, Y.Z, C.S, Q.W, Z.D, Y.L² and H.S performed the experiments. Z.Z, Y.Z, Q.W, W.L, Y.L² and H.S analyzed the data. Z.Z, Y.Z, C.S, Q.W, H.H, S.G, Y.L¹, R.T, L.C, Z.H, Y.L², H.S contributed materials/analysis tools. Z.Z, Y.Z, Z.S, Y.L², H.S wrote the paper.(Y.L¹: Yang Lv; Y.L²: Yubing Li.)

Competing interests: There are no competing interests to declare.

Data and materials availability: The data and codes that support this study are available in the website <https://open-waves-usct.github.io/>.

Supplementary materials

Supplementary Text

Figs. S1 to S3

Tables S1 to S12

Supplementary Materials for
***In vivo* 3D ultrasound computed tomography of musculoskeletal**
tissues with generative neural physics

Zhijun Zeng^{1,2,3†}, Youjia Zheng^{1,2†}, Chang Su^{4,5†}, Qianhang Wu^{1,2}, Hao Hu^{1,2},
Zeyuan Dong^{4,6}, Shan Gao⁷, Yang Lv⁷, Rui Tang⁸, Ligang Cui⁸,
Zhiyong Hou⁹, Weijun Lin^{4,5}, Zuoqiang Shi^{10,11*}, Yubing Li^{4,6*}, He Sun^{1,2*}

*Corresponding author. Z. Shi: zqshi@tsinghua.edu.cn, Y. Li: liyubing@mail.ioa.ac.cn, H.

Sun: hesun@pku.edu.cn

†These authors contributed equally to this work.

This PDF file includes:

Supplementary Text

Figs. S1 to S3

Tables S1 to S12

Supplementary Text

Conventional USCT Reconstruction Algorithm: Delay-and-Sum and Time of Flight Tomography

Delay-and-Sum (DAS) beamforming is one of the most fundamental and widely used techniques in real-time ultrasound imaging to reconstruct images from raw echo signals received by an array of transducer elements. It aligns and sums the delayed signals from each transducer element to focus on specific points within the imaging plane, thereby reconstructing a 2D structural image of the medium, which represents the echo intensity from tissue scattering. Under the full matrix capture (FMC) mode, the transmitting transducer element emits short pulses into the medium, and echoes are received by all transducer elements after bouncing off tissues at various scattering points. For every imaging point, DAS beamforming computes the traveltime from the emitting element to the point and back to each receiver—based on their distances and an assumed constant speed of sound—and applies the corresponding delays before summation. Specifically, in DAS imaging we employ the straight-ray (i.e. assuming constant sound speed) and the single-scattering approximations. Under these assumptions, the traveltime from the emitter to a target point and then to the receiver is given by

$$\tau_{s,r}(\mathbf{x}) = \frac{|\mathbf{x}_s - \mathbf{x}| + |\mathbf{x}_r - \mathbf{x}|}{c_0}, \quad (\text{S1})$$

where \mathbf{x} , \mathbf{x}_s and \mathbf{x}_r denote the coordinates of the imaging point, the source s , and the receiver r , respectively, and c_0 is the (spatially uniform) sound speed. The FMC data are beamformed to reconstruct the spatially varying echo image I , reading

$$I(\mathbf{x}) = \sum_{s=1}^{n_s} \sum_{r=1}^{n_r} d_{s,r}(\tau_{s,r}(\mathbf{x})), \quad (\text{S2})$$

where $d_{s,r}$ denotes the recorded signal of time series associated with source s and receiver r . Readers are referred to Perrot et al. (35) for more technical details.

Time of Flight Tomography (ToFT) is another powerful imaging technique that leverages ray propagation principles and Time of Flight (ToF) measurements to reconstruct the internal sound speed distribution of imaging targets. In this approach, the physical process is modelled by the

Eikonal equation

$$|\nabla T(\mathbf{x})| = \frac{1}{c^2(\mathbf{x})}, \quad (\text{S3})$$

where T is the traveltimes map from a source location \mathbf{x}_s to every location in space subject to the boundary condition of $T(\mathbf{x}_s) = 0$. Here, c is the spatially varying sound speed. The Eikonal equation can be resolved using fast marching or fast sweeping method.

In this work, we reconstruct the sound speed distribution c using the refraction-corrected ToFT algorithm. The goal is to find an optimal sound speed distribution map $c_{opt}(\mathbf{x})$, that best explains traveltimes measured associated with different source-receiver pairs on the ring transducer array. This objective is posed as a least-squares problem:

$$c_{opt} = \arg \min_c J_{toft}(c) = \frac{1}{2} \sum_{s=1}^{n_s} \sum_{r=1}^{n_r} |t_{s,r}^{cal}(c) - t_{s,r}^{obs}(c)|^2, \quad (\text{S4})$$

where $t_{s,r}^{cal}$ and $t_{s,r}^{obs}$ are calculated and observed traveltimes, respectively. The gradient of J_{toft} with respect to c is given by

$$\nabla_c J_{toft} = \sum_{s=1}^{n_s} \sum_{r=1}^{n_r} \frac{\partial t_{s,r}^{cal}}{\partial c} (t_{s,r}^{cal}(c) - t_{s,r}^{obs}(c)), \quad (\text{S5})$$

where $\frac{\partial t_{s,r}^{cal}}{\partial c}$ is related to the Jacobian matrix, describing how the ToF at a given point changes with respect to variations in the sound speed map c . These partial derivatives can be efficiently approximated using ray tracing on the traveltimes maps computed via the Eikonal equation. Once the gradient is obtained, the optimization problem is solvable through a gradient based method to estimate the optimal sound speed map c_{opt} that best fits the observed ToFs across different source-receiver pairs.

Implementation of Full Waveform Inversion optimization

We perform full waveform inversion for breast, leg, and arm imaging using a nonlinear conjugate gradient (NCG) optimizer. A hierarchical, multi-scale frequency-marching strategy is leveraged to reconstruct the scattering medium by solving inversion problems sequentially at progressively higher wave frequencies ω . Crucially, each sub-problem leverages the solution from the previous sub-problem as the initialization for the next optimization step. To avoid over-fitting, we apply a gaussian blurring filter to the output of the previous sub-problem before initiating the new one. To

ensure the selection of an appropriate initial step size, we normalize both the objective function and its gradient by their initial values within each sub-problem.

Given that the ultrasonic transmitters and receivers in the experimental setup share identical positions, the adjoint states can be directly obtained through a linear combination of the forward simulation results

$$\lambda_k(\mathbf{x}) = [u_i(\mathbf{x})]_i [u_i(\mathbf{x}_f^{(i)}) - y_k^{(i)}]_i^\top, \quad (\text{S6})$$

where $u_i(\mathbf{x})$ is the full acoustic wavefield corresponding to the i -th source, $\mathbf{x}_f^{(i)}$ defines the i -th source's location, $y_k^{(i)} \in \mathbb{C}$ is the recorded wavefield data of the i -th transducer. This technique significantly reduces computational costs.

The source intensity and phase of the ultrasound emitted by the instrument are often difficult to measure accurately. To mitigate this uncertainty, we performed source intensity estimation using linear regression during each gradient calculation. Notably, leveraging the linearity of the governing equations with respect to the source term, we used the point source in the forward simulations with unit intensity

$$\rho_k(\mathbf{x}) = \delta(\mathbf{x} - \mathbf{x}_f^{(k)}). \quad (\text{S7})$$

The estimated source was obtained by fitting the computed wavefield observation data $u_k(\mathbf{x}_f)$ to the measured observation data y_k :

$$\rho_k(\mathbf{x}) = \frac{\sum_{i=1}^K y_k^{(i)} \overline{u_k(\mathbf{x}_f^{(i)})}}{\sum_{i=1}^K u_k(\mathbf{x}_f^{(i)}) \overline{u_k(\mathbf{x}_f^{(i)})}} \delta(\mathbf{x} - \mathbf{x}_f^{(k)}). \quad (\text{S8})$$

Detailed Implementation of S^2NO

Encoder and Decoder: The S^2NO framework takes two input variables: wave speed c and input field $u_{\text{in}} = \rho$. The input field represents the wavefield generated by the transducer in a water medium for a given frequency and transducer location (i.e., the Helmholtz equation solution with homogeneous media). This input field encodes the frequency and source location of the current problem. We lift the input variables to high-dimensional feature spaces using linear encoders and project the output features of a series of nonlinear layers back to the physical space through MLP decoders. To emulate the Convergent Born Series (CBS) (20) in the feature space, we utilize three

linear encoders, $q = \mathcal{E}_{\theta_q}(c)$, $v = \mathcal{E}_{\theta_v}(c)$, $u_0 = \mathcal{E}_{\theta_{\text{init}}}(c, \rho)$, which introduce latent representations of $q(c) = 1 - i v(c)/\epsilon$, $v(c) = \left(\frac{\omega}{c(x)}\right)^2 - \kappa^2 - i\epsilon$, $u_0(\rho) = \mathcal{G}\rho$.

Based on extensive experiments with the network architecture, modifying the dependency of the latent representation u_0 to include both c and ρ improves performance. This adjustment does not undermine the interpretability or efficiency of S^2NO . We will further investigate the underlying reasons for this phenomenon.

Spectral Convolution Spectral convolution defines a powerful tool for parameterizing complex transformations. Let \mathcal{V} and \mathcal{U} denote the input and output function spaces of an operator $G : \mathcal{V} \rightarrow \mathcal{U}$, where any vector-valued function $v \in \mathcal{V}$ is defined as $v : \mathcal{D}_{\mathcal{V}} \rightarrow \mathbb{R}^{d_v}$ and any vector-valued function $u \in \mathcal{U}$ is defined as $u : \mathcal{D}_{\mathcal{U}} \rightarrow \mathbb{R}^{d_u}$. The spectral convolution operator G can be expressed as a linear integral operator:

$$(Gv)(x) := \int_{\mathcal{D}_{\mathcal{V}}} \kappa(x, y) v(y) dv(y), \quad (\text{S9})$$

where $\kappa(x, y)$ is a kernel function. To efficiently parametrize spectral convolution using neural networks, FNO³ reformulates this operation in the spectral domain and utilizes FFT to implement the integration. Assuming a translation-invariant kernel $\kappa(x, y) = \kappa(x - y)$ and applying the convolution theorem, the operator becomes:

$$(Gv)(x) = \mathcal{F}^{-1}(R \cdot \mathcal{F}(v))(x), \quad (\text{S10})$$

where \mathcal{F} and \mathcal{F}^{-1} denote the Fourier and inverse Fourier transforms, respectively. Since we assume that κ is periodic, we parametrize the kernel as a complex-valued tensor R and directly learn it from the data. For practical implementation, the Fourier series is truncated to a finite number of modes, with the maximum number of modes defined as:

$$k_{\max} = |Z_{k_{\max}}| = \left| \left\{ k \in \mathbb{Z}^d : |k_j| \leq k_{\max, j}, \text{ for } j = 1, \dots, d \right\} \right|.$$

The learned tensor R has a shape of $(k_{\max}, d_{\mathcal{V}}, d_{\mathcal{U}})$ tensor and the spectral multiplication is written as

$$(R \cdot \mathcal{F}(v_{\ell}))_{k,i} = \sum_{j=1}^{d_{\mathcal{V}}} R_{k,i,j} (\mathcal{F}(v_{\ell}))_{k,j}, \quad \forall k = 1, \dots, k_{\max}, i = 1, \dots, d_{\mathcal{U}}.$$

To ensure sufficient frequency coverage, we analyzed the spectrum of the wavefield and set $k_{\max} = 128$ across all experiments.

S^2NO Layer To emulate the Convergent Born Series in the feature space while maintaining the computational efficiency of back-propagation training, we design the S^2NO layer with the following formulation:

$$\begin{aligned} u_{n+1} &= BN(M_{\theta_M}(u_n, q, v) + u_0) \\ &= BN\left(\Phi_{\theta_M}\left((1 - q) \mathcal{F}^{-1} \circ R_{\theta_M} \circ \mathcal{F}(vu_n) + q u_n\right) + u_0\right), \end{aligned}$$

where BN refers to a BatchNorm2D layer, which is employed to accelerate the training of the deep learning model. In the S^2NO model, we utilize the same feature dimension for all layers. The function Φ_{θ_M} is implemented as a two-layer feed-forward network (FFN) with Leaky-ReLU activation. Our experiments revealed that incorporating this non-linearity enhanced the network’s ability to learn complex features.

Large scale training We trained eight S^2NO models, each tailored to data at a specific frequency. Each model was trained using data from 64 uniformly sampled sources out of a total of 256. All models were optimized with a relative L2 loss function

$$Relative\ L2 = \frac{\|u - \hat{u}\|_{L_2}}{\|u\|_{L_2}}, \quad (S11)$$

and trained on four NVIDIA A800-80 GB GPUs to ensure fairness. Detailed training parameters are provided in Table S1.

Implementation Details of Baselines

All the baselines were trained and tested under the same training strategy: We trained all forward simulation baseline models on the dataset of all three organs (breasts, arms, legs) for 30 epochs using the AdamW optimizer, with an initial learning rate of 5e-3, decayed by a StepLR scheduler. We used relative L2 loss for training and RRMSE for validation. See details in Table S1-S2. Next, we will present the implementation of all the baselines.

FNO To ensure a fair comparison, we used an FNO model with approximately the same number of parameters as the S^2NO model. Specifically, the encoder consists of a two-layer MLP. The Fourier layer employs mode=128 while maintaining a unified width=20. Finally, the decoder maps the latent variables back to the wavefield space using a two-layer MLP.

UNet We implemented the UNet using the same structure as in the work4 but a larger model size.

Neural Inverse Operator For inverse imaging, we adopted the Neural Inverse Operator (NIO) (11) model as a baseline for data-driven direct inversion and benchmarked it against neural operator-based FWI. NIO combines DeepONet with the FNO to enhance inversion accuracy, and leverages bagging method to improve generalizability. In our implementation, we adjusted the convolutional layer configurations in the branch network to accommodate USCT data. Specifically, the DeepONet trunk network comprises an eight-layer multilayer perceptron (MLP) with 100 hidden neurons per layer to generate 25 basis functions, while the branch network consists of a convolutional neural network (CNN) with 10 Conv2D layers followed by a linear layer to extract the coefficients of these basis functions. The FNO component comprises four Fourier layers with 40 modes and a width of 32.

DeepONet In this study, we implemented DeepONet for the Helmholtz equation following the architecture of the work (36): the branch network inputs the tensor $[c(x), Re(u_0(x)), Im(u_0(x))] \in \mathbb{R}^{3 \times 480 \times 480}$, which is processed by four 3×3 Conv2D layers with stride 2 that expand the channel dimension from 3 to 40, 60, 100 and finally 180; the resulting feature maps are then flattened and passed through a three-layer MLP with hidden sizes of $[180, 80, 80]$ to produce the coefficients of the basis functions, while the trunk network takes the 2D coordinate $x \in \mathbb{R}^2$ and projects it via a fully connected network with three hidden layers of 80 units each to generate the corresponding basis functions.

Implementation Details for Fine-tuning Stable Diffusion Model

Training Stage During the training stage, we randomly selected 200/600/200 2D phantom samples of the breast, arm, and leg, obtained using physics-based generation, and converted them into grayscale images. The breast phantom samples comprise equal proportions of four categories: heterogeneous (HET), fibroglandular (FIB), all-fatty (FAT), and extremely dense (EXD). We fine-tuned the Stable Diffusion v1.4 model using Dreambooth (34) method, with training parameters provided in Table S3.

Generation Stage During the generation stage, we utilized the DDIM scheme for text-to-image generation with the fine-tuned model, employing the training prompt. The generated samples were subjected to a plausibility evaluation, including assessments of organ size, bone count, and skin thickness. Subsequently, image processing and segmentation were performed to extract different tissues, and sound speed values were assigned to the segmented regions accordingly. This workflow enabled us to successfully produce high-quality 2D phantoms of breast, arm, and leg.

Evaluation Metrics

We evaluated the performance of the baseline methods independently for the forward simulation and inverse imaging tasks, using RRMSE for the former and PSNR and SSIM for the latter.

Relative RMSE (RRMSE) for forward simulation Given the ground-truth physics field u and the model predicted field \hat{u} , the RRMSE can be calculated as follows:

$$RRMSE = \frac{1}{M} \sum_{i=1}^M \frac{\|u_i - \hat{u}_i\|_{L2}}{\|u_i\|_{L2}}. \quad (S12)$$

SSIM for inverse imaging Given the ground-truth sound speed c and the reconstructed sound speed \hat{c} , the SSIM of the reconstruction result can be calculated as follows:

$$SSIM(c, \hat{c}) = \frac{(2\mu_c\mu_{\hat{c}} + C_1)(2\sigma_{c\hat{c}} + C_2)}{(\mu_c^2 + \mu_{\hat{c}}^2 + C_1)(\sigma_c^2 + \sigma_{\hat{c}}^2 + C_2)} \quad (S13)$$

where $\mu_c, \mu_{\hat{c}}$ are means of c and \hat{c} , $\sigma_{cc}, \sigma_{\hat{c}\hat{c}}$ are their variances, $\sigma_{c\hat{c}}$ is their covariance, and C_1, C_2 are small constants to stabilize the division.

Evaluation of the model performance on Synthetic Dataset

After training on the synthetic dataset, we evaluated the forward simulation accuracy of our models and baseline models.

Breast Supplementary Fig. S1 displays the wavefield predictions at 0.6 MHz for all models across four distinct breast types, while Supplementary Table S6 reports the RRMSE of each model for every category in the test set. Our results demonstrated that S^2NO outperformed all competing baselines

at every frequency, accurately capturing the complex scattering phenomena—particularly at the skin–air interface. Furthermore, both quantitative metrics and qualitative assessments confirmed that S^2NO preserved its accuracy when applied to out-of-distribution *in vivo* breast tissue, whereas alternative approaches exhibited limited generalizability.

Arm Supplementary Fig. S2 presents the 0.6 MHz wavefield predictions by different models for a physics-based generated arm phantom, a stable diffusion generated arm phantom and an *in vivo* human arm. S^2NO outperformed all baseline methods, exhibiting particularly high accuracy in strongly scattering regions such as bone cavities and the boundary. The RRMSE for each model on these samples, summarized in Supplementary Table S7, further supported this conclusion. Prediction accuracy on the arm dataset was comparatively higher, owing to reduced scattering effects in the smaller arm geometry. Nevertheless, our model retained exceptional generalizability, achieving an RRMSE of 10.2% at 0.6 MHz.

Leg Supplementary Fig. S3 presents the 0.6 MHz wavefield predictions provided by different models for a physics-based generated leg phantom, a stable diffusion–generated leg phantom and an *in vivo* human leg. The RRMSE for each model on these samples is summarized in Supplementary Table S8. Compared to the arm, the leg featured larger scales and more substantial bone structures, resulting in stronger scattering effects. Our S^2NO model demonstrated superior accuracy on both in-distribution phantoms and out-of-distribution clinical sample, accurately capturing scattering phenomena within bone cavities—an aspect vital to the reconstruction quality of musculoskeletal tissues. In contrast, FNO incurred errors of up to 40% at high frequencies, highlighting its inability to effectively exploit high-frequency information in the reconstruction process.

Runtime Evaluation

Supplementary Table S10 presents the forward simulation times of CBS, S^2NO and other baseline models at 0.3 MHz and 0.6 MHz. Here, the forward simulation time refers to the computational time required to compute the wavefields for all 256 transducers of a single phantom, with a batch size of 64. All data points were obtained from 100 independent simulations performed on ten randomly selected phantoms.

Supplementary Table S11 summarizes the inverse imaging times for synthetic breast, arm, and leg phantoms using CBS, S^2NO , and other baseline models. For breast phantoms, we performed a one-round reconstruction using data at seven frequencies (0.3–0.6 MHz). For arm and leg phantoms, we carried out a two-round reconstruction with data at eight frequencies (0.25–0.6 MHz), using the first round’s output—after Gaussian blurring—as the initial model for the second round. All data points were obtained from independent experiments on 5 randomly selected phantoms. For forward simulations, the batch size for all neural-network models was set to 32. Model loading and compilation times were excluded from the reported durations, as these steps can be completed before the actual imaging process.

Supplementary Table S12 summarizes the inverse imaging times for *in vivo* human breast, arm, and leg datasets using CBS, S^2NO , and other baseline models. Computation times were measured on two *in vivo* breast datasets, for which reconstructions were performed using data at seven frequencies (0.3–0.6 MHz). Similarly, computation times were evaluated on 11 *in vivo* arm/leg datasets, each reconstructed using data at eight frequencies (0.25–0.6 MHz). The parameters for forward simulation and inference timing were identical to those employed for synthetic data.

All the tests were performed on the same device and platform, which is a Linux desktop (Ubuntu 398 20.04.3 LTS operation system) with Intel(R) Xeon(R) Platinum 8358P CPU @ 2.60GHz and a single NVIDIA A800-80GB (Driver Version: 520.61.05, CUDA Version: 11.8). All the computational time costs are listed in Supplementary Table S5.

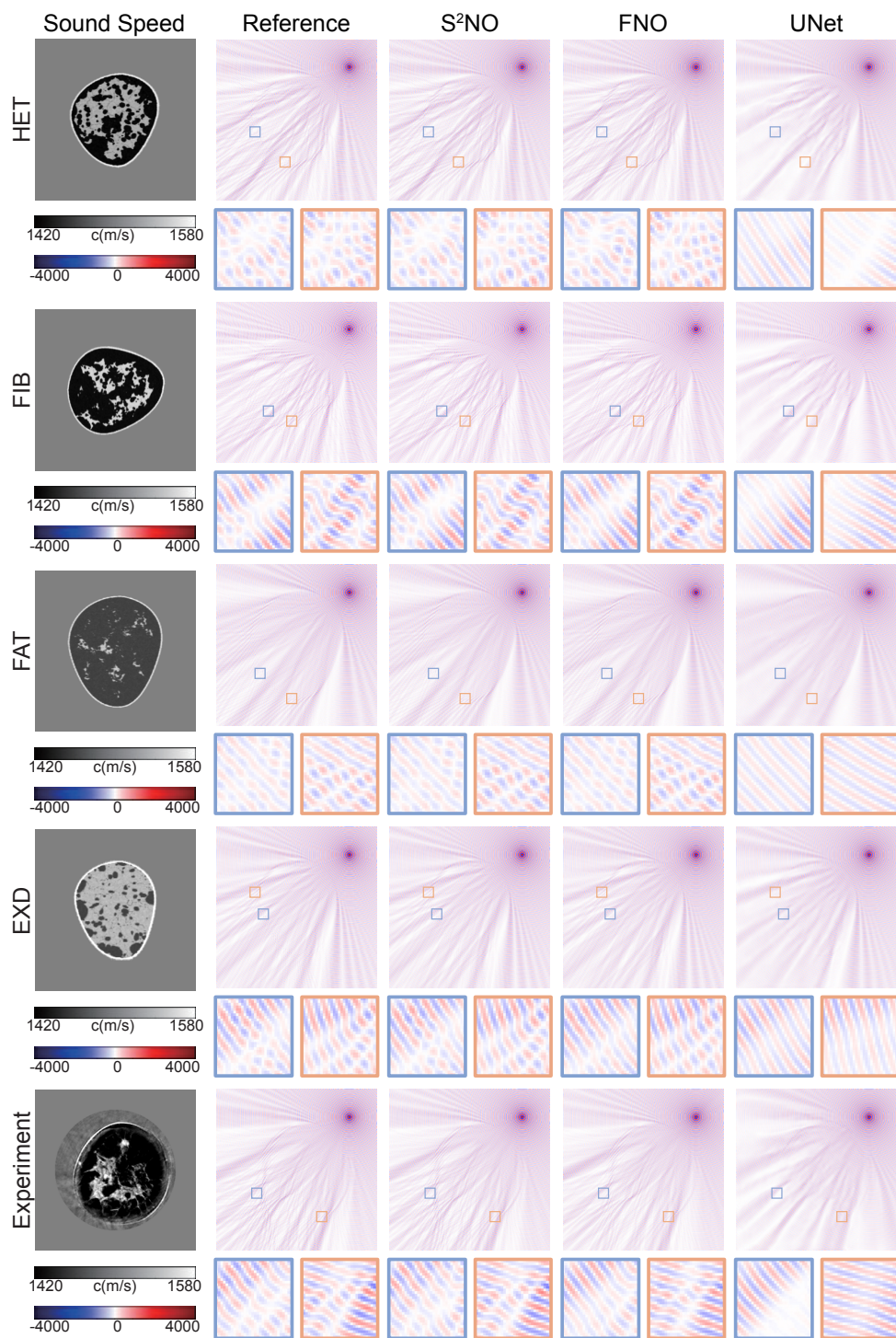


Figure S1. Forward simulation results for four types of breast phantoms and one *in vivo* human breast.

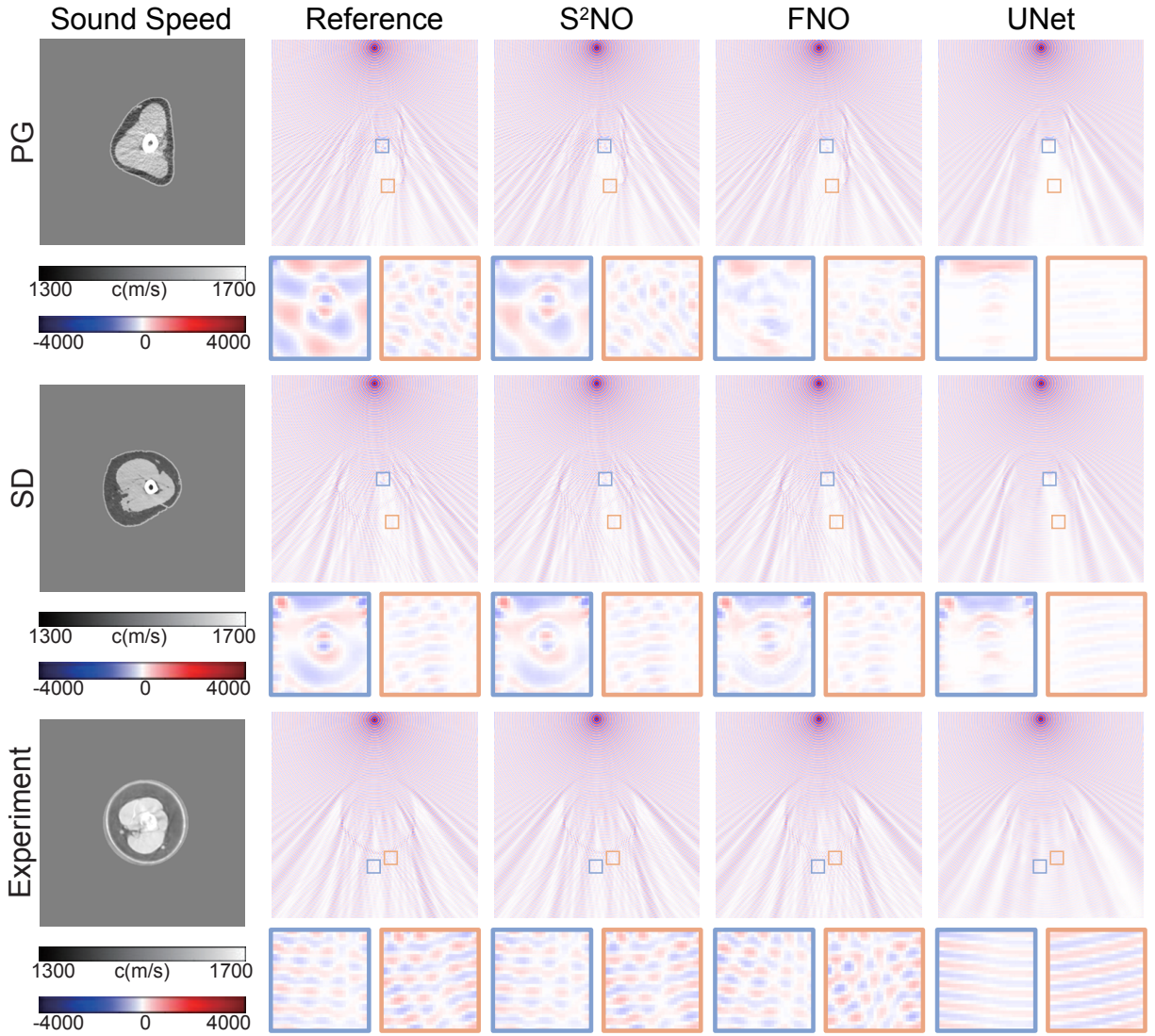


Figure S2. Forward simulation results for physics-based and Stable Diffusion generated arm phantoms and an *in vivo* human arm.

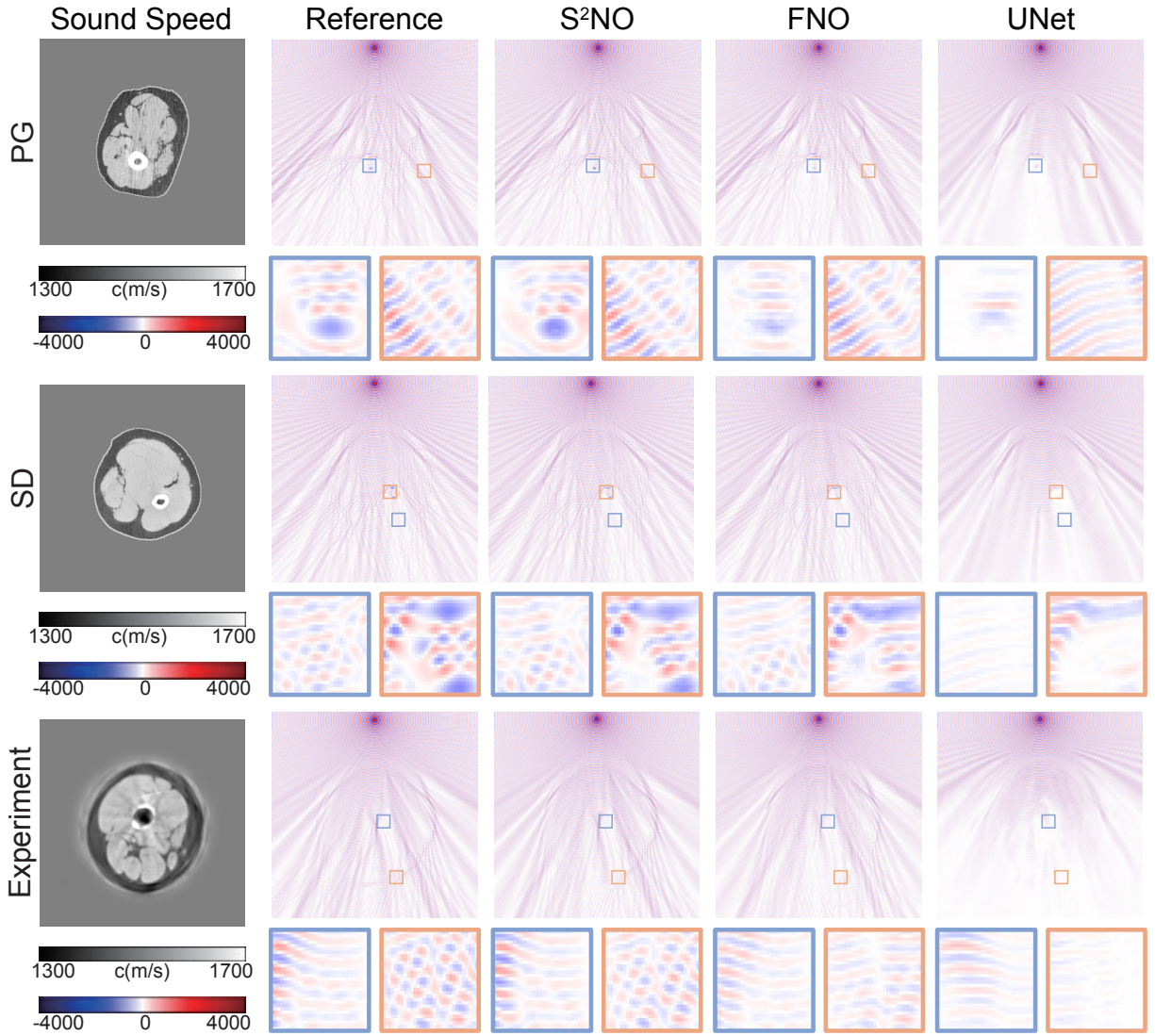


Figure S3. Forward simulation results for physics-based and Stable Diffusion generated leg phantoms and an *in vivo* human leg.

Table S1. Hyperparameter list for the implementation of S^2NO

Parameters		0.25~0.6 MHz
Model Structure	modes	128
	widths	20
	layer number	7
	padding	6
	fc_v	(3,20,20)
	fc_u0	(5,20)
	fc_q	(3,20,20)
	fc_out	(20,256,2)
	optimizer	AdamW
	learning rate	0.005
Training Process	step size	6
	gamma	0.1
	weight_decay	0.00001

Table S2. Hyperparameter list for training the baseline models

Model	Parameters	0.25~0.6 MHz
FNO	Widths	20
	Modes	128
	MLP encoder	(5,20)
	MLP decoder	(3,20)
UNet	Input channel	3
	Output channel	2
	Skip channel	4
	Depth	16
	Channels	[60×4, 120×4, 240×4, 480×4]
	Activation	LeakyReLU
	Norm	GroupNorm
DeepONet	Trunk MLP	(2,80,80,80)
	Activation	ReLU
	BranchNet	4 Conv2D (3×3,channels [3,40,60,100,180]) + MLP(180,80,80)
	Basis Number	80
	Output MLP	(80,2)
NIO	Trunk MLP	(2,100,100,100,100,100,100,100,100,100)
	Activation	GeLU
	BranchNet	10×Conv2D + MLP(100,25)
	Basis Number	25
	Modes	40
	Width	32

Table S3. Finetuning/inference parameters of Stable Diffusion

Finetune Parameter	Value
Pretrained Model	stable-diffusion-v1.4
mixed_precision	fp16
resolution	480
train_batch_size	1
gradient_accumulation_steps	3
gradient_checkpointing	True
learning_rate	1e-4
snr_gamma	5.0
lr_scheduler	constant
lr_warmup_steps	0
max_train_steps	4000
Inferencing Parameter	Value
Scheduler	DDIM
Step	50
Scheduler	DDIM

Table S4. Summary of breast dataset

Data Source	Breast Type	Frequency (MHz)	Phantoms	Storage
VICTRE	Heterogeneous (HET)	0.25~0.6	880	773GB
	Fibroglandular (FIB)		880	773GB
	Fatty (FAT)		880	773GB
	Extremely Dense (EXD)		880	773GB
Stable Diffusion	Heterogeneous (HET)	0.25~0.6	1000	879GB
	Fibroglandular (FIB)		1000	879GB
	Fatty (FAT)		1000	879GB
	Extremely Dense (EXD)		1000	879GB

Table S5. Summary of arm/leg dataset

Organ	Data Source	Frequency (MHz)	Phantoms	Storage
Arm	X-ray CT Conversion	0.25~0.6	809	711GB
	Stable Diffusion		6717	5.77TB
Leg	X-ray CT Conversion	0.25~0.6	1001	880GB
	Stable Diffusion		6000	5.15TB

Table S6. Forward simulation errors of breast phantoms at 8 frequencies

Frequency (MHz)	Metric	Model			
		S ² NO	FNO	UNet	DeepONet
0.25	RRMSE(Val)	0.016	0.036	0.187	0.771
	RRMSE(Exp)	0.034	0.089	0.258	0.891
0.3	RRMSE(Val)	0.025	0.048	0.210	0.803
	RRMSE(Exp)	0.049	0.114	0.295	0.925
0.35	RRMSE(Val)	0.033	0.061	0.234	0.822
	RRMSE(Exp)	0.067	0.145	0.326	0.954
0.4	RRMSE(Val)	0.043	0.072	0.244	0.835
	RRMSE(Exp)	0.085	0.157	0.348	0.931
0.45	RRMSE(Val)	0.049	0.087	0.269	0.844
	RRMSE(Exp)	0.094	0.189	0.405	0.928
0.5	RRMSE(Val)	0.057	0.101	0.281	0.851
	RRMSE(Exp)	0.104	0.206	0.406	0.935
0.55	RRMSE(Val)	0.067	0.113	0.302	0.856
	RRMSE(Exp)	0.131	0.222	0.444	0.931
0.6	RRMSE(Val)	0.077	0.134	0.310	0.862
	RRMSE(Exp)	0.139	0.263	0.454	0.926

Table S7. Forward simulation errors of arm phantoms at 8 frequencies

Frequency (MHz)	Metric	Model			
		S ² NO	FNO	UNet	DeepONet
0.25	RRMSE(Val)	0.029	0.051	0.183	0.531
	RRMSE(Exp)	0.015	0.038	0.217	0.574
0.3	RRMSE(Val)	0.040	0.068	0.201	0.540
	RRMSE(Exp)	0.021	0.052	0.465	0.580
0.35	RRMSE(Val)	0.052	0.079	0.218	0.545
	RRMSE(Exp)	0.028	0.084	0.338	0.521
0.4	RRMSE(Val)	0.058	0.087	0.222	0.546
	RRMSE(Exp)	0.039	0.109	0.294	0.648
0.45	RRMSE(Val)	0.066	0.100	0.236	0.548
	RRMSE(Exp)	0.053	0.130	0.268	0.653
0.5	RRMSE(Val)	0.075	0.108	0.243	0.552
	RRMSE(Exp)	0.063	0.132	0.342	0.657
0.55	RRMSE(Val)	0.071	0.113	0.255	0.556
	RRMSE(Exp)	0.068	0.142	0.393	0.668
0.6	RRMSE(Val)	0.077	0.123	0.260	0.560
	RRMSE(Exp)	0.102	0.186	0.348	0.676

Table S8. Forward simulation errors of leg phantoms at 8 frequencies

Frequency (MHz)	Metric	Model			
		S ² NO	FNO	UNet	DeepONet
0.25	RRMSE(Val)	0.042	0.078	0.248	0.733
	RRMSE(Exp)	0.054	0.164	0.773	0.878
0.3	RRMSE(Val)	0.062	0.104	0.271	0.737
	RRMSE(Exp)	0.076	0.205	0.527	0.878
0.35	RRMSE(Val)	0.080	0.122	0.293	0.744
	RRMSE(Exp)	0.096	0.226	0.734	0.899
0.4	RRMSE(Val)	0.099	0.139	0.304	0.757
	RRMSE(Exp)	0.170	0.269	0.606	0.970
0.45	RRMSE(Val)	0.106	0.161	0.326	0.773
	RRMSE(Exp)	0.138	0.300	0.507	0.915
0.5	RRMSE(Val)	0.118	0.181	0.336	0.760
	RRMSE(Exp)	0.146	0.316	0.398	0.905
0.55	RRMSE(Val)	0.127	0.195	0.358	0.764
	RRMSE(Exp)	0.183	0.342	0.512	0.904
0.6	RRMSE(Val)	0.139	0.213	0.361	0.767
	RRMSE(Exp)	0.187	0.419	0.547	0.916

Table S9. Reconstruction quality of breast/arm/leg phantoms using different models

Organ	Metric	Model			
		CBS	S ² NO	FNO	UNet
Breast	SSIM↑	0.951 ± 0.052	0.958 ± 0.031	0.938 ± 0.034	0.921 ± 0.029
Arm	SSIM↑	0.980 ± 0.006	0.978 ± 0.007	0.971 ± 0.008	0.974 ± 0.009
Leg	SSIM↑	0.969 ± 0.005	0.966 ± 0.006	0.958 ± 0.013	0.892 ± 0.038

Table S10. Evaluation of runtime for forward simulation

Model	Frequency	#Parameter	Inference time [s]		
			Breast	Arm	Leg
S ² NO	All	367M		1.3052 ± 0.0002	
FNO	All	367M		0.6102 ± 0.0002	
UNet	All	25M		0.8404 ± 0.0004	
DeepONet	All	5M		0.02290 ± 0.00001	
CBS	0.3 MHz	/	7.619 ± 0.430	19.241 ± 2.610	21.773 ± 1.183
CBS	0.6 MHz	/	13.718 ± 2.847	31.894 ± 4.891	44.734 ± 7.443

Table S11. Evaluation of runtime for inverse imaging process of synthetic data

Inverse Imaging of synthetic data				
Model	# Parameters	Imaging process time [s]		
		Breast	Arm	Leg
S ² NO	367M	176.56 ± 25.12	393.29 ± 8.08	482.87 ± 13.73
FNO	367M	109.84 ± 11.60	260.15 ± 19.78	290.26 ± 17.18
UNet	25M	149.00 ± 20.33	281.09 ± 3.77	334.45 ± 93.93
CBS	/	963.04 ± 37.35	5807.95 ± 160.85	6308.23 ± 496.15

Table S12. Evaluation of runtime for inverse imaging process of experimental data

Inverse Imaging of experimental data				
Model	# Parameters	Imaging process time [s]		
		Breast	Arm	Leg
S ² NO	367M	466.85 ± 74.76	510.29 ± 16.39	567.32 ± 38.76
CBS	/	3045.78 ± 65.48	3506.59 ± 110.36	7995.62 ± 684.14